Gravity recovery from SWOT altimetry using geoid height and geoid gradient

Yu, Daocheng; Hwang, Cheinway; Andersen, Ole Baltazar; Chang, Emmy T.Y.; Gaultier, Lucile

Published in:
Remote Sensing of Environment

Link to article, DOI:
10.1016/j.rse.2021.112650

Publication date:
2021

Document Version
Publisher's PDF, also known as Version of record

Remote Sensing of Environment 265 (2021) 112650

Contents lists available at ScienceDirect

Remote Sensing of Environment

journal homepage: www.elsevier.com/locate/rse

Gravity recovery from SWOT altimetry using geoid height and geoid gradient

Daocheng Yu [a], Cheinway Hwang [a,*], Ole Baltazar Andersen [b], Emmy T.Y. Chang [c], Lucile Gaultier [d]

[a] Department of Civil Engineering, National Yang Ming Chiao Tung University, 1001 Ta Hsueh Road, Hsinchu 300, Taiwan
[b] DTU Space, Technical University of Denmark, Kgs. Lyngby 2800, Denmark
[c] Institute of Oceanography, National Taiwan University, No. 1, Sec. 4, Roosevelt Road, Taipei 106, Taiwan
[d] OceanDataLab, 870 Route de Deolen, 29280 Locmaria Plouzané, France

ARTICLE INFO

Editor by: Menghua Wang

Keywords:
Surface water and ocean topography (SWOT) mission
Marine gravity
Geoid gradient
Geoid height
Inverse Stokes' integral
Inverse Vening-Meinesz formula
South China Sea

ABSTRACT

The Surface Water and Ocean Topography (SWOT) altimeter mission can measure high-resolution wide-swath sea surface heights (SSHs) that may greatly improve the current accuracy and spatial resolution of marine gravity from nadir-looking altimeters. To investigate the potential of SWOT in recovering high-quality marine gravity and how SWOT observation errors should be treated to optimize the accuracy of gravity anomaly from SWOT observations, we create high-wavenumber SSH components from multi-beam depths in the northern South China Sea (SCS) and simulate SWOT SSH errors. To cross-validate gravity signals and avoid gravity errors from SWOT, we use two computational methods (inverse Vening-Meinesz formula, IVM and inverse Stokes' integral, ISM) and recommend separate optimal data processing strategies when using geoid gradients (GGs) and geoid heights (GHs) for gravity recovery. The use of GGs (for IVM) effectively eliminates systematic errors in gravity derivation. If GHs (for ISM) are used in gravity recovery, the tilt in wide-swath SSHs should be removed before gravity computation, and the recovered gravity must be filtered (post-processed) to avoid artificial gravity signals due to the SSH errors. Our assessments using mgal-accuracy shipborne gravity anomalies in the northern SCS show that multiple-cycle SWOT observations can deliver high-quality marine gravity anomalies. IVM is more robust than ISM in resisting random and systematic errors in SWOT. Our processing strategies can be used for the gravity validation of SSHs from SWOT's fast-sampling and science phases.

1. Introduction

With the ever-increasing data quality and volume of satellite altimeter data, marine gravity recovered from altimetry is well into a new era. However, along-track sea surface heights (SSHs) from nadir-looking altimeters are severely limited in providing high-resolution and coherent marine gravity fields and consequently seafloor structures (Andersen et al., 2010; Escudier et al., 2013; Sandwell and Smith, 2001). For example, the along-track resolution of nadir altimeters is about 6 km with a one-HZ sampling rate, but the cross-track spacing of exact repeat missions (ERM) can be over 100 km, depending on the repeat period. Although the cross-track spacing of multiple geodetic missions (GMs) can be reduced to a few km, the accuracy of these missions can be decreased because of a lack of exact repeated measurements for stacking to enhance the quality of SSH observations. Several studies showed that, the root-mean-squared (RMS) differences between shipborne and satellite-derived marine gravity fields (DTU10, DTU15, DTU17, V23.1, V27.1, V28.1) may be about 5 mgal (Watts et al., 2020; Zhang et al., 2017; Zhu et al., 2020). The nominal grid intervals of these fields are 1×1 min, but the actual signal resolution (half-wavelength) may exceed 6 km (Andersen and Knudsen, 2019; Sandwell et al., 2019). These problems in altimeter-derived gravity may soon be alleviated with the launch of the Surface Water Ocean Topography (SWOT) altimeter mission in February 2022 (Fu and Ubelmann, 2014). Unlike a nadir-looking altimeter (named "conventional altimeter" below), SWOT's major payload, a Ka-band Radar Interferometer (KaRIN) altimeter, will measure surface elevations over a 120-km wide swath with a 20-km gap around the nadir track. According to Morrow et al. (2019a), SWOT's wide-swath spatial resolution from the Level 2 ocean products is 2 km, enabling a high-precision and high-accuracy mapping of surface

* Corresponding author at: Department of Civil Engineering, National Yang Ming Chiao Tung University, 1001 Ta Hsueh Road, Hsinchu 300, Taiwan.
E-mail address: cheinway@nctu.edu.tw (C. Hwang).

https://doi.org/10.1016/j.rse.2021.112650
Received 29 December 2020; Received in revised form 10 August 2021; Accepted 12 August 2021
Available online 18 August 2021

elevations for hydrological, oceanographic, and geophysical studies. In theory, SSHs from SWOT can lead to a marine gravity field with a uniform (omnidirectional) and unprecedented (< 2 km) spatial resolution that cannot be achieved using along-track SSHs from conventional altimeters, including recent synthetic aperture radar (SAR)-based altimeters such as Sentinel-3A, Sentinel-3B and Cryosat-2.

There have been many studies on the applications of SWOT elevation observations to surface water hydrology and oceanography. Sample hydrological applications of SWOT are about hydrology simulations (Elmer et al., 2020), hydrology error budget (Biancamaria et al., 2010), river discharge (Huang et al., 2020; Larnier et al., 2020; Tuozzolo et al., 2019), river bathymetric depth and slope (Durand et al., 2008), river reach definition (Frasson et al., 2017), and surface water storage (Lee et al., 2010; Solander et al., 2016). Oceanographic research using SWOT data includes SWOT observation simulation (Gaultier et al., 2016), observation error elimination (Gómez-Navarro et al., 2020, 2018), mission calibration and validation (Wang et al., 2018; Wang and Fu, 2019), and data assimilation (D'Addezio et al., 2019; Lopez-Radcenco et al., 2018), among other works. However, except the discussion by Louis et al. (2010), there is little research about the potential use of SWOT measurements for marine gravity derivation.

Marine gravity anomalies can be derived from geoid heights (GHs) or geoid gradients (GGs). A GH in the ocean is an SSH without dynamic oceanic topography (DOT), which is the separation between the sea surface and the geoid. GHs can be converted to marine gravity anomalies by methods based on the inverse Stokes' integral (Molodenskii et al., 1962; Wang, 2001, 1999), and numerically implemented in either the spatial and frequency domain (Andersen and Knudsen, 1998, 1996; Knudsen et al., 1992; Olgiati et al., 1995). GGs can be converted to marine gravity anomalies using the relationship between gravity and the north and east slope components of the geoid, which can be implemented by numerical methods that take advantage of the fast Fourier transform (FFT) (Olgiati et al., 1995; Sandwell, 1992; Sandwell and Smith, 1997; Schwarz et al., 1990), by least-squares collocation (LSC) (Hsiao et al., 2016; Hwang and Parsons, 1995), or by the method of inverse Vening-Meinesz (IVM) (Hwang, 1998; Hwang et al., 2002; Hsiao et al., 2016). In theory, GGs are less contaminated by long-wavelength errors in the original SSHs and this is of particular importance when along-track SSHs are affected by biases and slopes (Olgiati et al., 1995).

Because the SWOT mission can provide two-dimensional elevations at land and sea at spatial scales not achievable by current nadir-looking (along-track) altimeters, the objective of this paper is to investigate the potential of SWOT SSH observations in recovering marine gravity anomalies, and then recommend the data processing strategies when GGs or GHs are used for gravity recovery. Two independent methods, IVM and method of inverse Stokes' integral (ISM) based on GGs and GHs separately, will be used in this paper to ensure that the recovered marine gravity field from future SWOT data is cross-validated and reliable. The study area is in the northern South China Sea (SCS), where multi-beam depth measurements and high-quality shipborne gravity anomalies are available to help identify an ideal data processing procedure for gravity recovery. Simulated SWOT SSHs were generated by combining the DTU18 mean sea surface (DTU18MSS; available at https://www.space.dtu.dk) with the high-wavenumber SSH components generated from multi-beam depth measurements, in an approach following the concept of residual terrain model (RTM) in geoid modeling (Forsberg, 1984). We used realistic error models of SWOT measurements (Gaultier et al., 2016) to simulate major errors of SWOT. However, errors caused by wind and wave, such as sea-state bias and ocean swells, were not modeled because of a lack of such error models. We examined how such errors impact the recovered marine gravity and how they can be mitigated. All the abbreviations used in this paper are listed in Appendix A.

2. Depth and gravity measurements for SWOT simulation and gravity accuracy assessment

2.1. Multi-beam depth dataset and bathymetry dataset from GEBCO

To generate high-wavenumber SSHs mimicking SWOT observations, we obtained a high-quality multi-beam depth dataset measured by multi-beam echo-sounders in the northern SCS from the Ministry of the Interior (MOI), Taiwan (Hsiao et al., 2016). A multi-beam sonar emits short acoustic pulses toward the sea floor to scan the depths over a field of view. The multi-beam depths have a nominal spatial resolution of 500 m and a mean accuracy of few meters. Fig. 1 (a) shows the depths from this dataset. Most of the multi-beam depths in this dataset were collected in the area south of Dongsha (Pratas) Island (20°42′N, 116°43′E), with extensions to the Bashi Channel north of the Philippines. There are no multi-beam depths in areas west of the Philippines (the void zone). The depths in this void zone were filled by the depths from the 2020 version of the General Bathymetric Chart of the Oceans (the GEBCO_2020 grid) (URL: http://www.gebco.net; see also Weatherall et al., 2014). The GEBCO_2020 grid contains the bathymetry of the world's oceans on a 15″ × 15″ grid. Fig. 1 (b) shows the differences between the depths from the multi-beam dataset and from the GEBCO_2020 grid. The differences are mainly attributed to high-frequency seafloor features such as seamounts and trenches detected by the multi-beam measurements, which are not present in the GEBCO grid. Fig. 2 shows the depths from a combination of these two datasets, which are regarded as the true depths when simulating SWOT-observed SSHs (Section 3.1).

2.2. Shipborne gravity anomalies

We obtained the along-track shipborne gravity anomalies collected over 2009–2016 from the Ocean Data Bank of Taiwan. The shipborne gravity data were measured by the gravimeter LaCoste & Romberg Air-Sea Gravity System II (S/N: S150) onboard Taiwan's R/V Ocean Researcher I (ORI), in marine surveys for the northern SCS. The mean and the standard deviation of the crossover difference are 2.3 and 2.2

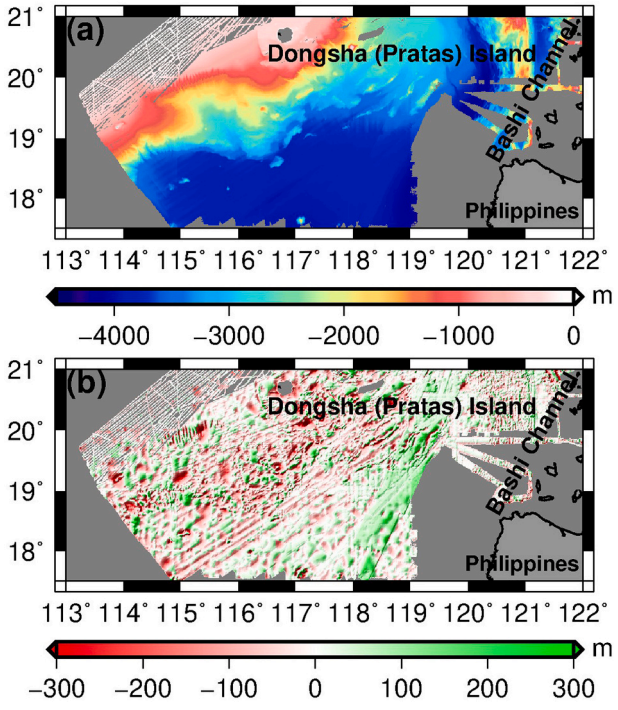

Fig. 1. (a) Depths from the multi-beam dataset, with the areas without depth measurements (void zone) shaded by gray, and (b) the differences between the depths from the multi-beam dataset and from the GEBCO_2020 grid.

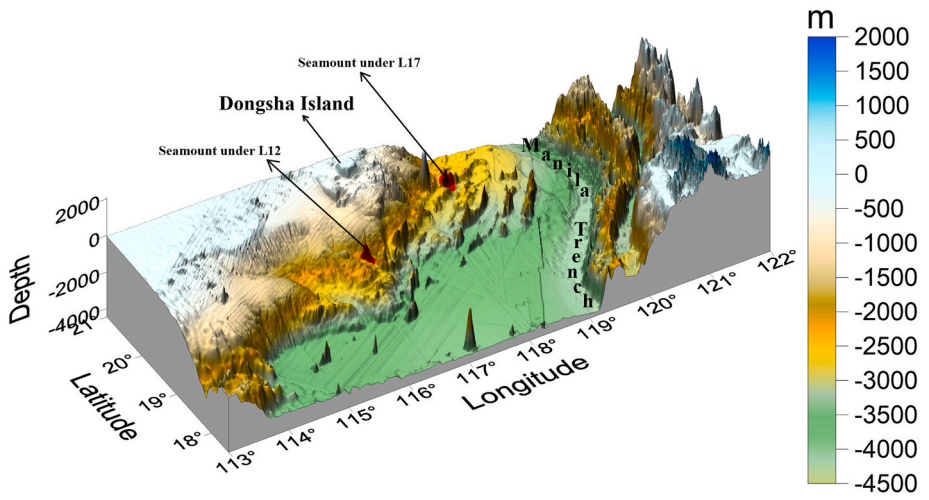

Fig. 2. Seafloor topography in the northern South China Sea from multi-beam depths and the GEBCO_2020 grid. Two red circles enclose the two seamounts along L12 and L17 discussed in Section 5. (For interpretation of the references to colour in this figure legend, the reader is referred to the web version of this article.)

mgal, respectively (Lee et al., 2016). Fig. 3 shows the distribution of the shipborne gravity data. For the assessment of the gravity anomalies from the SWOT measurements, we used the gravity field of the Earth Gravitational Field Model 2008 (EGM2008; Pavlis et al., 2012) to degree 2160 as a reference field to remove the bias and tilt of the shipborne measurements in each of the cruises using a time-dependent quadratic polynomial (Hwang and Parsons, 1995).

3. Simulating SWOT-measured SSHs with characteristic errors

3.1. Simulating high-wavenumber SSHs using multi-beam depths

The SWOT mission will use a radar interferometer to measure high-resolution SSHs, which can change the way we observe oceanic dynamic topography and oceanic geoidal undulations assuming they can be separated from each other. Currently, there is no SSH model whose spatial resolution and accuracy are consistent with those expected from the SWOT SSH measurements for a realistic test of the potential of SWOT observations in recovering fine gravity signatures originating from fine seafloor structures. The DTU18MSS model is the latest MSS from DTU Space, but the filter used for generating this model may reduce signal strengths over rugged topographic features, including seamounts that can produce bumps on the GHs by exerting additional gravitational forces to the level surface around the seamounts (Fu and Cazenave, 2000). In this paper, we derived the expected signatures of the seamounts on the MSS (name "high-wavenumber SSH components" below) from the multi-beam depths (Section 2.1), which were then superimposed on DTU18MSS to simulate the SSHs from SWOT. As shown in Fig. 4, the high-wavenumber SSH components are generated using

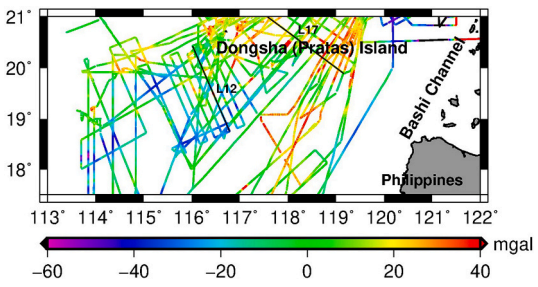

Fig. 3. Shipborne gravity anomalies in the northern South China Sea (SCS), archived and edited by the Ocean Data Bank of Taiwan. Two black lines represent L12 and L17 discussed in Section 5.

$$H_{RDM}(x_p, y_p) = \frac{G}{\gamma}\int_{y_1}^{y_2}\int_{x_1}^{x_2}\frac{\rho(x,y)\big(h(x,y)-h_{ref}(x,y)\big)}{\sqrt{(x-x_p)^2+(y-y_p)^2}}dxdy$$
$$= \frac{G}{\gamma}\left[\rho\left(h-h_{ref}\right)\right]*\frac{1}{r} \quad (1)$$

where H_{RDM} is called the residual depth model (RDM) effect on SSH, G is the gravitational constant, γ is normal gravity, (x_1, x_2) and (y_1, y_2) define the west-east and south-north limits of the integration for RDM in the local x-y plane centered at P, $\rho = 1.64$ g · cm^{-3} is density contrast (difference between the densities of rock and seawater), h is the true depth, h_{ref} is the reference depth, $= \sqrt{x^2+y^2}$, and * is the convolution operator.

The concept of RDM (Fig. 4) is similar to that of residual terrain model (RTM) that can account for the high-frequency geoid components due to rapid topographic variations (Forsberg, 1984). The residual depth is the difference between the true depth and the reference depth (Fig. 4). The true depth at a given point is interpolated from the combined multi-beam and GEBCO_2020 depths (Fig. 2). The reference depth is obtained by low-pass filtering the true depth with a wavelength of 20 km and is shown in Fig. 5 (a). Double integrating the residual depths by Eq. (1) can model the high-wavenumber SSH components (Fig. 5 (c)). The horizontal and vertical stripes in Fig. 5 (c) are artifacts, which are small compared to the gravity signals and can be ignored.

The high-wavenumber SSH components have the same spatial frequency as that of the residual depths and are meant to compensate for the missing high-wavenumber SSHs in DTU18MSS, which has half-wavelength resolution of 6–8 km. A high-frequency variation in SSH usually coincides with variation in seafloor topography of a commensurate spatial frequency. As shown in Fig. 5 (c), large, high-wavenumber SSHs are present over the shallow waters of the northern SCS, where the seafloor topography fluctuates rapidly.

The DTU18MSS has a nominal sampling of 1 min (about 2 km in the northern SCS) and was used as the starting surface over which high-wavenumber SSH components from multi-beam depths are superimposed. The SSH measurements (ellipsoidal heights of sea surface) of SWOT can be generated by

$$H_{SWOT} = H_{DTU18} + H_{RDM} + \varepsilon \quad (2)$$

where H_{SWOT} is from SWOT, H_{DTU18} is from DTU18MSS, H_{RDM} is the high-wavenumber, SWOT-sensed SSH component by Eq. (1), and ε is a simulated SWOT observation error (Section 3.2).

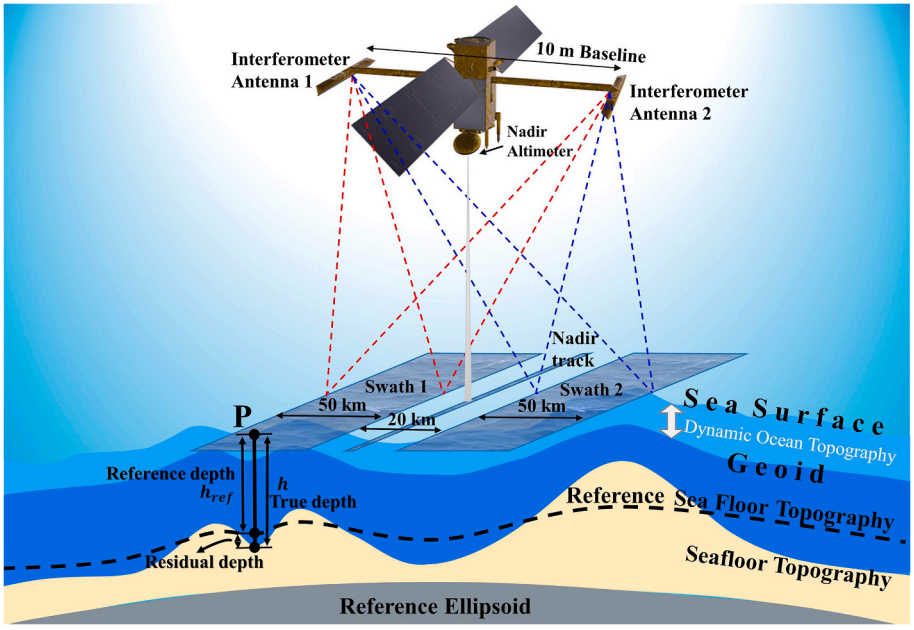

Fig. 4. Illustrations of SWOT SAR measurements of SSH over the two swaths and nadir track, and the residual depth (RDM) generated by differencing the true depth (Fig. 2) and a reference depth (a low-pass filtered true depth, Fig. 5 (a) below) that can be sensed by SWOT.

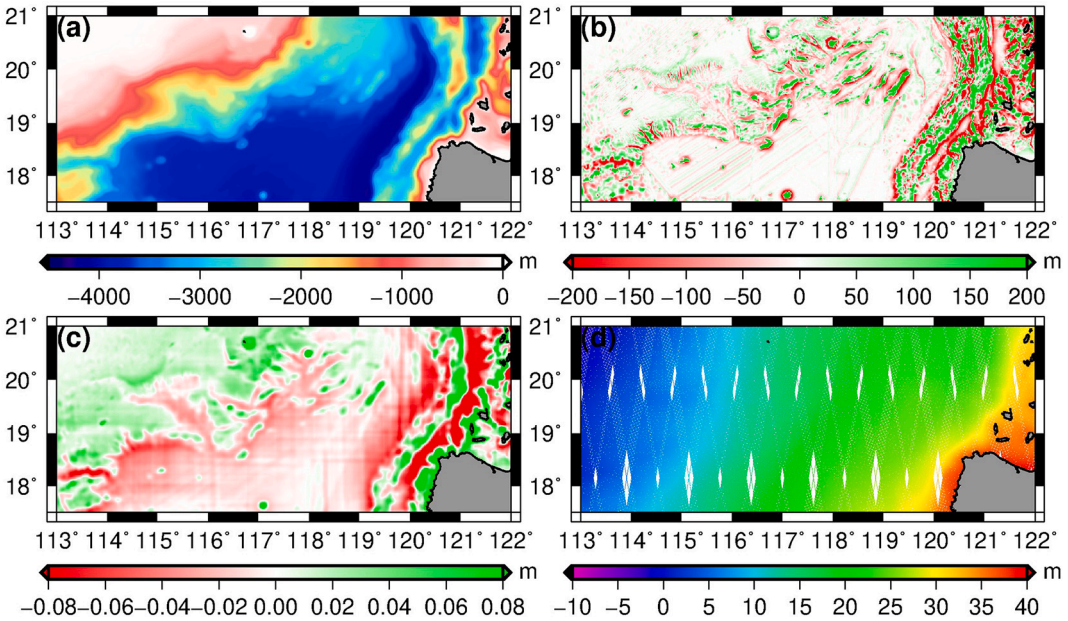

Fig. 5. (a) Reference depths, (b) residual depths, (c) high-wavenumber SSH components, and (d) simulated error-free SWOT SSH observations (called SSH_model; one cycle SWOT data). The data gaps are caused by the 20-km void zones adjacent to the nadir tracks (Fig. 4).

3.2. The characteristic errors of SWOT SSHs

We used the SWOT simulator (version 3.1) developed by Gaultier et al. (2016) to simulate SWOT SSH observations. First, the simulator constructed a SWOT observation grid of SSH (Fig. B1) over the swath coverage in the northern SCS defined by the SWOT science orbits. Currently, the nominal two-dimensional sampling interval of the SWOT Level 2 ocean products is set to 2 km. Therefore, we determined the 2 km × 2 km grid points in the along- and cross-track directions over the swaths and the 2-km interval points along nadir tracks. Second, the SWOT simulator interpolated the input SSH model on the grid points to generate error-free SWOT SSH observations. Third, the SWOT observation errors were created by the SWOT simulator and then added to the error-free SSHs to generate error-contaminated SWOT SSH observations.

Using the SWOT simulator, we generated three sets of SWOT SSH observations. The first set contains SSHs only from DTU18MSS (H_{DTU18}, called SSH_DTU18). The second set contains error-free SWOT observations (called SSH_model, Fig. 5 (d)) from the sums of SSHs from DTU18MSS and from the high-wavenumber SSHs ($H_{DTU18} + H_{RDM}$). The third set contains error-contaminated SWOT observations (called SSH_obs), which are the sums of SSHs from SSH_model and the simulated SWOT errors ($H_{DTU18} + H_{RDM} + \varepsilon$). In this study, we generated nineteen, 21-day-repeat cycles of SWOT SSH observations (about 400 days) aimed to recover marine gravity.

The SWOT simulator generated SSH errors over the coverages of the nadir-looking and the SAR altimeters according to the error budget of

SWOT (Esteban-Fernandez, 2017). The SSH errors over the SAR swaths include instrument errors and geophysical correction model errors (called geophysical errors for short below). The instrument errors include the KaRIN error, roll error, phase error, baseline dilation error, and timing error (Gaultier et al., 2016). Fig. 6 (a) - (e) show these errors in the northern SCS. In this paper, only one major geophysical error, the wet tropospheric delay error (Fig. 6 (f)), was simulated by the simulator using the method of Ubelmann et al. (2014). The remaining geophysical corrections, including dry troposphere and ionosphere errors, were not applied because their error magnitudes are relatively small compared to that of the wet tropospheric delay error. Details about all the simulated SSH errors of SWOT can be found in Esteban-Fernandez (2017) and Gaultier et al. (2017).

Compared with a conventional altimeter, the SWOT SAR altimeter will experience an instrument error caused by its SAR. According to the interferometric measurement concept in Fig. 7 (a), the ellipsoidal height at a sea surface point (h) can be approximated as

$$h \approx H - r \bullet \cos\Theta \tag{3}$$

where H is the ellipsoidal height of the SWOT antenna, Θ is the look angle, and r is the range from the antenna to the sea surface point. The roll error (δΘ) is an error caused by the error of the antenna roll angle (Θ, Fig. 7 (b)) and results in the height error (δh) at a sea surface point as (Esteban-Fernandez, 2017)

$$\delta h = r \bullet \sin(\Theta)\delta\Theta \approx C\left(1 + \frac{H}{R_E}\right)\delta\Theta \tag{4}$$

where C is the cross-track distance from the point to SWOT's nadir track and R_E is the radius of the Earth (about 6371 km). Eq. (4) suggests that the roll-induced height error increases linearly with the cross-track distance from the nadir track toward the swath edge. The roll-induced errors over a swath form a tilted, erroneous surface with respect to the true sea surface over the swath (Esteban-Fernandez, 2017; Rodriguez et al., 2018), as shown in Fig. 7 (b).

The two SAR images from the paired KaRIN antennas can form an interferogram containing phase differences. At a given pixel, the error in the phase difference, δϕ, can introduce a height error given by (Esteban-Fernandez, 2017)

$$\frac{\delta h = -\lambda \bullet r \bullet tan(\Theta)}{2\pi B\,\delta\phi \approx \frac{C}{kB}\left(1 + \frac{H}{R_E}\right)\delta\phi} \tag{5}$$

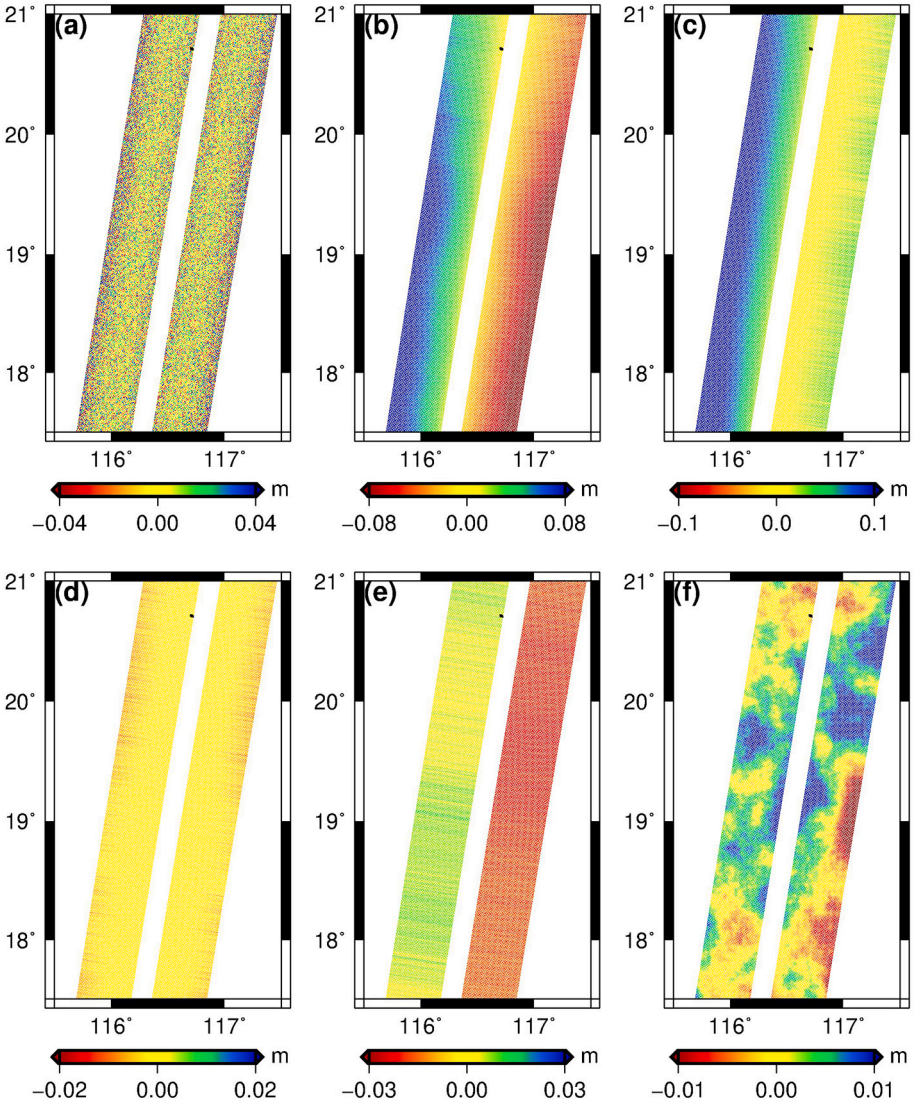

Fig. 6. The SWOT observation errors over the swaths of pass 135 simulated by the SWOT simulator. (a) The KaRIN instrument error, (b) the roll error, (c) the phase error, (d) the baseline dilation error, (e) the timing error, and (f) the wet tropospheric delay error. Errors in (a) appear random, while errors in (b)-(e) are of systematic nature.

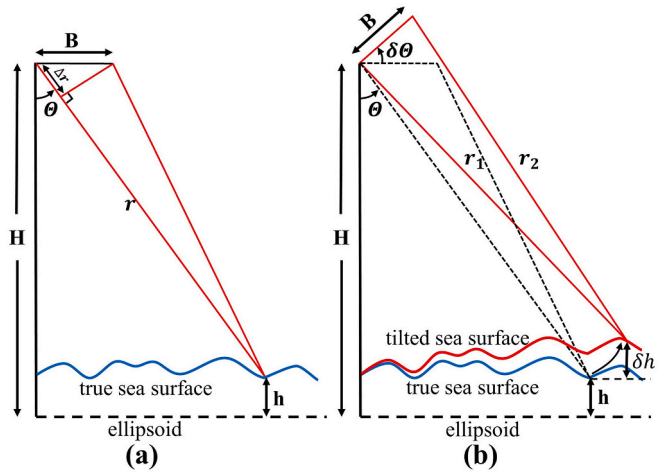

Fig. 7. Illustration of (a) the interferometric measurement concept and (b) a titled sea surface (in red) due to the roll error (δΘ). H is the ellipsoidal height of the SWOT antenna, Θ is the look angle, r_1 and r_2 are the range distances from two antennas to a sea surface point, B is the length of baseline, Δr is the difference between r_1 and r_2, which is obtained from the phase difference between the two radar channels, h is the height of a point on the sea surface, and δh is the height error due to δΘ. (For interpretation of the references to colour in this figure legend, the reader is referred to the web version of this article.)

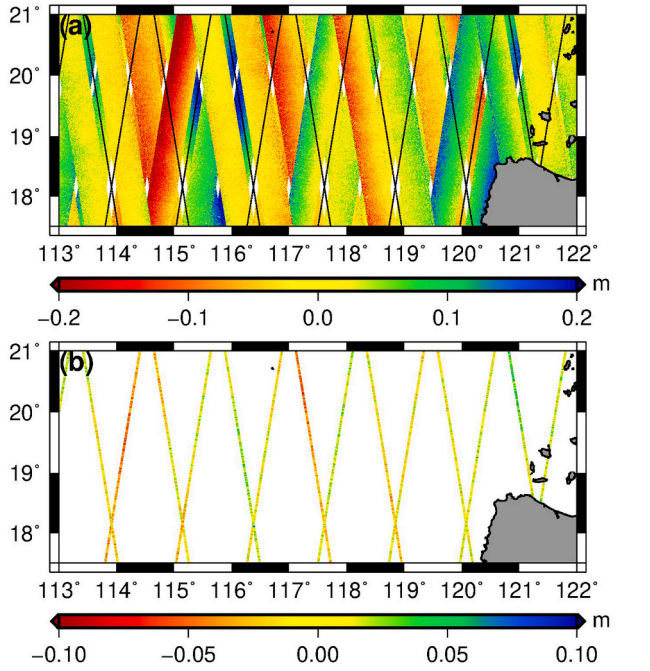

Fig. 8. Simulated one-cycle SSH errors of SWOT over (a) swaths and (b) nadir tracks in the northern SCS. Black lines in (a) represent the nadir tracks.

where λ is the wavelength of the radar and k is the electromagnetic wavenumber. Like the roll error, the phase error also increases linearly across the swath. Furthermore, the baseline dilatation error δB, which is a change in the baseline length, will introduce height errors as (Esteban-Fernandez, 2017)

$$\delta h = -\frac{r \bullet sin(\Theta) tan(\Theta)}{B}\delta B \approx -\left(1+\frac{H}{R_E}\right)\frac{C^2}{HB}\delta B \tag{6}$$

The presence of C^2suggests that the baseline-dilatation-induced height errors increase quadratically across the swath. Finally, the height error introduced by a system timing error (δt) is (Esteban-Fernandez, 2017)

$$\delta h = -cos(\Theta)\delta r \approx \frac{c}{2}cos(\Theta)\delta t \tag{7}$$

where c is the speed of light. The timing error is constant with respect to the look angle Θ.

The simulated SSH errors over all the swaths in the northern SCS are shown in Fig. 8 (a). The pattern of the SSH errors in Fig. 8 (a) is consistent with that predicted by the theories above: the SSH errors increase with the distances from the nadir track. Specifically, for each pass, these errors form a tilted sea surface around the nadir track, and different passes have different tilts. In addition to tilts, other minor systematic errors and random errors can introduce high-frequency SSH noises. In addition, Fig. 8 (b) shows the SSH errors over the nadir tracks, which are mainly originated from the instrument (the nadir altimeter) and from the wet tropospheric delay error.

It is important to note that the SWOT simulator in this paper only simulated the most important systematic errors related to the roll and length variation of the baseline of the two antennas (Fig. 4), and the errors in range (or timing) and phase. There could be several errors not modeled here. As pointed out by Esteban-Fernandez (2017), a major intrinsic noise can arise from the interferometer. Also, errors in satellite orbits, as well as the spatial variabilities of the waves and wind fields of the SWOT-observed sea surface will also introduce additional height errors (Esteban-Fernandez, 2017). As pointed out by Sandwell and Smith (2001), ocean waves, including ocean swells, can introduce additional errors to marine gravity recovered from SWOT altimeter data as it is for conventional altimetry. Such ocean wave-induced errors will be analyzed when the real SWOT data are available.

4. Marine gravity recovery methods

4.1. Method of inverse Vening-Meinesz (IVM) using geoid gradients

When using IVM, the remove-compute-restore procedure was used to avoid global integrations (Forsberg, 1984). First, the simulated two-dimensional SWOT SSH observations in the two swaths on the two sides of the nadir track were split into one-dimensional along- and cross-track observations (as shown in Fig. B1). Second, the DOT from Levitus et al. (1997) was removed from the SWOT SSHs. According to Hwang et al. (2002) and Andersen et al. (2010), we can ignore DOT gradients in the northern SCS creating artificial gravity signals in altimeter-derived gravity anomalies. Third, the GHs of EGM2008 to degree 2160 were removed from the GHs to generate the residual GHs. The residual GHs were then used to compute the residual GGs (negative deflection of the vertical, DOV) by

$$\varepsilon_{\alpha,res} = \frac{(N_{res2} - N_{res1})}{d} \tag{8}$$

where the $\varepsilon_{\alpha,\,res}$ is the residual GG with azimuth α, N_{res1} and N_{res2} are two successive residual GHs in both the along- and cross-track directions (Appendix B), and d is their distance. The geodetic latitude and longitude of the GG in Eq. (8) are at the central location of N_{res1} and N_{res2}, thus the numerical differentiation in Eq. (8) corresponds to the central-difference approximation (Gerald, 2004). We have experimented with several methods for deriving GGs. One method is fitting SSHs by a polynomial first, followed by numerical differentiations of this polynomial. However, this method can easily amplify the errors of the resulting GGs with polynomial degrees higher than 2. One way to reduce error amplification is by filtering SSHs before numerical differentiations (Section 5.1). Because the focus in this paper is to show the potential of SWOT in deriving high-frequency gravity signals, optimizing the numerical differentiation of GGs is not discussed here.

The residual GGs can be used to form the north and east components of GGs on a grid using the method of least-squares collocation (LSC; Hwang and Parsons, 1995) or the method of Sandwell and Smith (1997).

In this paper, we used LSC for forming the north and east gradient components. Appendix B shows the theory and numerical method for constructing grids of north and east gradient components, which can be converted to residual gravity anomalies by the inverse Vening-Meinesz formula (Hwang, 1998):

$$\Delta g_P = \frac{\gamma_0}{4\pi}\iint_\sigma H'\left(\xi_Q cos\alpha_{QP} + \eta_Q sin\alpha_{QP}\right)d\sigma_Q \tag{9}$$

where P is the computational point, Q is a contributing point on the unit sphere, Δg_P is the residual gravity anomaly at P, γ_0 is the normal gravity, σ is the unit sphere, ξ_Q and η_Q are the north-south and west-east components of the residual GGs at Q, α_{QP} is the azimuth from Q to P, H' is a kernel function of the spherical distance between Q and P (Hwang, 1998), and $d\sigma_Q$ is the areal element of the unit sphere σ. With the north and east gradient components given on a regular grid, Eq. (9) can be implemented using one-dimensional FFT (Hwang, 1998). By restoring the reference gravity values of EGM2008 to the residual gravity anomalies computed by Eq. (9), the full marine gravity anomalies can be obtained.

We also consider the innermost-zone effect around the neighborhood of the computational point (P), where the kernel function H' is nearly or completely singular. The innermost-zone effect on the gravity anomaly is

$$\Delta g_i = \frac{s_0\gamma_0}{2}\left(\xi_y + \eta_x\right) \tag{10}$$

where $\xi_y = \partial\xi/\partial y$ and $\eta_x = \partial\eta/\partial x$, ($x$ and y are the rectangular coordinates pointing east and north, respectively) are the gradients of the GGs, and s_0 is the radius of the innermost zone, which can be approximated from the grid intervals, Δx and Δy, as:

$$s_0 = \sqrt{\frac{\Delta x \Delta y}{\pi}} \tag{11}$$

In this paper, ξ_y and η_x were obtained by numerical differentiations of ξ and η along the y and x directions using routine "QD2DR" in the International Mathematical and Statistical Library (IMSL) package by fitting a 12 × 12 window of grid around the grid point where ξ_y and η_x are evaluated.

4.2. Method of inverse Stokes' integral (ISM) using geoid heights

The two-dimensional wide-swath SWOT SSH observations can be interpolated onto a regular grid for direct gravity recovery, but it is not clear how errors in SSHs could degrade the gravity accuracy. We assessed this issue using ISM. Here, GHs are converted to gravity anomalies by the inverse Stokes' integral (Molodenskii et al., 1962)

$$\Delta g_P = -\frac{\gamma_0 N_P}{R} - \frac{\gamma_0 R^2}{2\pi}\iint_\sigma \frac{N_Q - N_P}{l_0^3}d\sigma_Q \tag{12}$$

where Δg_P is the residual gravity anomaly at the computational point P, R is the mean radius of the Earth, $l_0 = 2Rsin(\Psi_{PQ}/2)$ is the distance between P and the contributing point Q (Ψ_{PQ} is the spherical angle between P and Q), and N_Q and N_P are the GHs at Q and P, respectively. A planar FFT formula for the computation of the second term in Eq. (12) is given by Olgiati et al. (1995). Alternative spectral-domain formulae for the second term in Eq. (12) were suggested by, e.g., Forsberg and Solheim (1989), Forsberg and Sideris (1993), and Andersen and Knudsen (1998, 1996). Wang (2001) used a space-domain formula for the integration in Eq. (12).

Like IVM, ISM was also implemented by the remove-compute-restore procedure to avoid global integrations. In this procedure, the geoid height N is be replaced by the residual GH. In this paper, the integration of the second term in Eq. (12) was made using the Gaussian quadrature over a cap around P (see Appendix C for the numerical detail). The Gaussian quadrature for the second term in the inverse Stokes' integral is similar to that used for terrain correction (Hwang et al., 2003). It is more rigorous than an FFT-based method, but is slower computationally.

When Q is near P, l_0 approaches zero, and then the kernel in Eq. (12) becomes singular. This singularity was avoided by neglecting the contribution at P (that is, Q = P), e.g., Wang (2001). However, we consider this contribution by computing the innermost-zone effect for the inverse Stokes' integral. This effect is derived following the approach for Stokes' formula (Heiskanen and Moritz, 1967), where the innermost zone comes from the contribution from points over a plane around P. In the polar coordinates, the areal element on a sphere of radius R is

$$R^2 d\sigma = sdsd\alpha \tag{13}$$

where s and α are the distance and azimuth from P to P's neighboring point. Around the neighborhood of P, the geoid height N can be expanded into a Taylor series as:

$$N = N_P + xN_x + yN_y + \frac{1}{2!}\left(x^2N_{xx} + 2xyN_{xy} + y^2N_{yy}\right) + \ldots \tag{14}$$

where $N_x = \partial N/\partial x$, $N_y = \partial N/\partial y$, $N_{xx} = \partial^2 N/\partial x^2$, $N_{yy} = \partial^2 N/\partial y^2$, and $x = s \cdot sin\,\alpha$ and $y = s \cdot cos\,\alpha$ are the rectangular coordinates pointing east and north, respectively. Eq. (14) can also be written as

$$N = N_P + s\left(sin\alpha N_x + cos\alpha N_y\right) + \frac{1}{2}\left(s^2sin^2\alpha N_{xx} + 2s^2sin\alpha cos\alpha N_{xy} + s^2cos^2\alpha N_{yy}\right) + \ldots \tag{15}$$

Thus

$$N - N_P = s\left(sin\alpha N_x + cos\alpha N_y\right) + \frac{1}{2}\left(s^2sin^2\alpha N_{xx} + 2s^2sin\alpha\cos\alpha N_{xy} + s^2cos^2\alpha N_{yy}\right) + \ldots \tag{16}$$

The innermost zone is assumed to be a circle of radius s_0 around P, as defined by Eq. (11). With Eq. (12), the contribution to gravity anomaly from the innermost zone is

$$\begin{aligned}\left(\Delta g_P\right)_i &= -\frac{\gamma_P}{2\pi}\int_{\alpha=0}^{2\pi}\int_{s=0}^{s_0}\frac{1}{s^3}\left[s\left(sin\alpha N_x + cos\alpha N_y\right) + \frac{1}{2}\left(s^2sin^2\alpha N_{xx} + 2s^2sin\alpha\cos\alpha N_{xy} + s^2cos^2\alpha N_{yy}\right) + \ldots\right]sdsd\alpha \\ &= -\frac{\gamma_P}{4\pi}\left(N_{xx}\int_{\alpha=0}^{2\pi}sin^2\alpha d\alpha\int_{s=0}^{s_0}ds + N_{yy}\int_{\alpha=0}^{2\pi}cos^2\alpha d\alpha\int_{s=0}^{s_0}ds + \ldots\right) \\ &= -\frac{\gamma_P s_0}{4}\left(N_{xx} + N_{yy} + \ldots\right)\end{aligned} \tag{17}$$

Retaining only the first term, we have

$$\left(\Delta g_P\right)_i = -\frac{\gamma_P s_0}{4}\left(N_{xx} + N_{yy}\right) \tag{18}$$

where N_{xx} and N_{yy} are obtained by the second-order numerical differentiations of N along the x and y directions by QD2DR. The s_0 term in Eq. (18) is the same as that given in Eq. (11). Fig. 9 shows the innermost-zone effects in IVM and ISM. The gravity magnitudes in Fig. 9 can be larger than one mgal in areas with large variations in seafloor topography (Fig. 2). The results in Fig. 9 (a) and (b) suggest that the innermost-zone effect should be considered if we wish to achieve a mgal-level marine gravity accuracy when using either GGs or GHs for gravity recovery.

5. Gravity recovery from simulated SWOT observations

5.1. Gravity recovery from error-free and error-contaminated SWOT SSHs by IVM

Using IVM (Section 4.1), we derived gravity anomalies from the simulated SWOT observations (Section 3.2). Note that all the SSHs in the

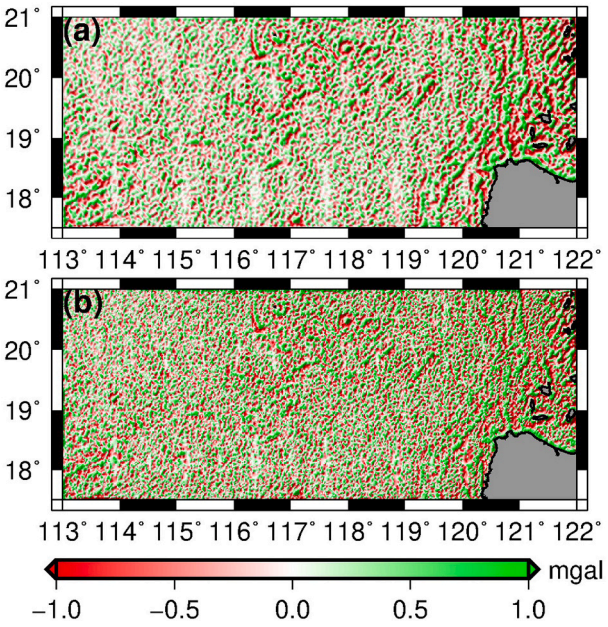

Fig. 9. The innermost-zone gravity effect from SSH_model by (a) IVM (using GGs), and (b) ISM (using GHs).

results below are free from the effect of DOT and can be considered as geoid heights at sea (Section 4.1). To verify the fidelity of the simulated SWOT observations and the effect of SWOT errors on the derived marine gravity anomalies, first, we experiment with gravity recovery using only one cycle (21-day) of SWOT observations. Then, we use 19 cycles (about 1 year) of SWOT observations to examine error reductions in the gravity fields.

We derived gravity anomalies from one cycle of error-free SWOT observations (SSH_model), as shown in Fig. 10 (a), and from SSH_DTU18 by IVM. The differences between them are shown in Fig. 10 (b) and are attributed to the high-wavenumber SSH components (Fig. 5 (c)). The signals in Fig. 10 (b) are similar to those in Fig. 5 (b) and (c). The stripes in Fig. 10 (b) are caused by the small artifacts in Fig. 5 (c). To see how two-dimensional SSHs from SWOT to resolve gravity details, we did an experimental case in which gravity anomalies were determined using only along-track SSHs (Fig. B1). The differences between the gravity using only along-track SSH_model and both along- and cross-track SSH_model are shown in Fig. 10 (c). The differences are mainly attributed to the east gradient components (η): because the inclination angle of SWOT's orbit is 77.6°, the azimuth of SWOT's cross-track direction in study area (northern SCS) is about 102.4°, which helps to resolve the east gradient components from cross-track SSHs and enhance gravity signals. The differences between the gravity anomalies in Fig. 10 (a) and those from the error-contaminated SWOT observations (SSH_obs) are shown in Fig. 10 (d). The differences indicate the effect of SWOT errors on the recovered gravity. Relatively large differences (Fig. 10 (d)) occur at the edges of swaths, where the errors in the SWOT observations are larger (Fig. 8 (a)).

The quality of the recovered gravity anomalies was assessed using the shipborne gravity anomalies presented in Section 2.2. For this assessment, we used only ship measurements along 19 straight-trajectory lines over shallow waters (Fig. 11 (a); Section 2.2). For example, Fig. 11 (b) and (c) show respectively two profiles of gravity anomalies and depths along L12 and L17 (here, L means a straight-line segment along a cruise). In Fig. 11 (b), the rising seafloor (the summit is at 19.5°N; Fig. 2) between the two vertical red dashed lines indicate a seamount that results in larger gravity anomalies than its neighborhood. Along L12, gravity anomalies from all cases are consistent within a few mgal, except near the summit of the seamount. Along L17, the depths and gravity anomalies undergo relatively large variations between the two red vertical dashed lines enclosing a seamount (the summit is at 20.5°N; Fig. 2) in Fig. 11 (c). At around 20.32°N-20.45°N along L17, the shapes of the gravity anomalies from both the SWOT altimetry and ship measurements are concaved, in contrast to the flat seafloor here. The gravity concaves are the result of the seamount-induced lithospheric flexures. The flat seafloor here is caused by the sediments that filled the flexures around the seamount (Watts, 2001, p. 130). In fact, gravity concaves and a flat seafloor also occur on the two flanks of the seamount of L12 in Fig. 11 (b), but with smaller gravity magnitudes.

Over the seamounts (the areas enclosed by the two red vertical dashed lines in Fig. 11 (b) and (c)), the high-wavenumber SSH components from SWOT (generated by the residual depths in Section 3.1) improve the accuracies of the SWOT-recovered gravity anomalies. For example, the gravity anomalies from the error-free SWOT observations (SSH_model, the blue dashed lines) are much closer to the shipborne values (the cyan lines), compared with the results from SSH_DTU18 (the green lines). As shown in Table 1, the RMS differences between the altimetry and shipborne gravity values in the case of SSH_model (3.15

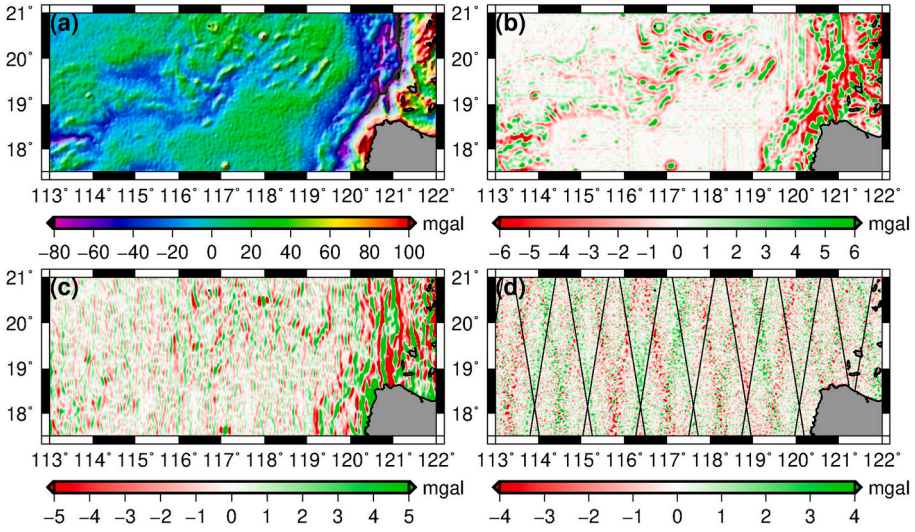

Fig. 10. (a) Gravity anomalies from one cycle of SSHs (SSH_model) by IVM, (b) differences between gravity anomalies from SSH_model and SSH_DTU18 (effect of high-wavenumber SSH components), (c) differences between gravity anomalies from only along-track SSH_model and along- and cross-track SSH_model, and (d) differences between gravity anomalies from SSH_model and SSH_obs (effect of SWOT errors). Black lines in (d) represent the nadir tracks.

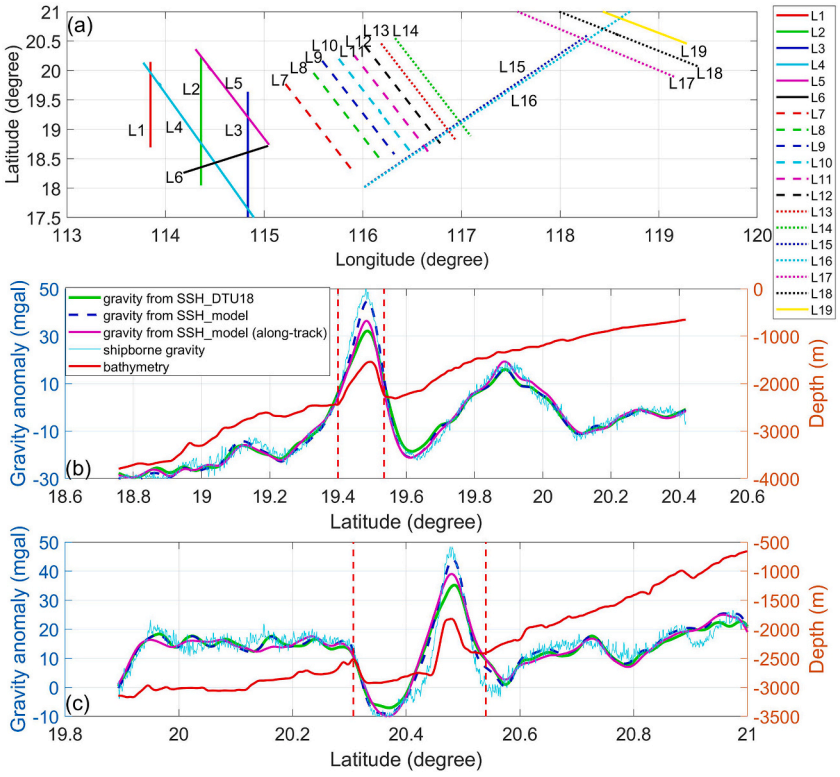

Fig. 11. (a) Distribution of nineteen straight-trajectory lines of shipborne gravity anomalies, (b) depths and IVM-derived gravity anomalies (one-cycle SWOT data) along L12, and (c) L17.

Table 1
RMS differences between the IVM-derived gravity anomalies (one-cycle SWOT data) and the shipborne gravity anomalies over the seamounts under L12 and L17 (unit: mgal).

Line	Gravity from	RMS	Maximum	Minimum
	DTU17 gravity	7.18	2.01	−23.65
	SSH_DTU18	5.74	2.45	−17.94
L12	SSH_model	3.15	4.76	−8.26
	SSH_model (along-track)	3.42	−0.87	−13.5
	SSH_obs	3.59	6.79	−6.97
	DTU17 gravity	6.49	13.98	−14.34
	SSH_DTU18	6.05	12.99	−14.26
L17	SSH_model	3.58	10.93	−5.33
	SSH_model (along-track)	5.47	14.23	−9.52
	SSH_obs	3.7	12.03	−5.83

mgal and 3.58 mgal for L12 and L17) are significantly smaller than those in the case of SSH_DTU18. Table 2 shows the RMS differences for all 19 lines (Fig. 11 (a)). In Table 2, Rate1 is defined as $\frac{RMS_{SSH\_DTU18} - RMS_{SSH\_model(along\&cross)}}{RMS_{SSH\_DTU18}} \times 100\%$, which represents the effect of high-wavenumber SSH components. The high-wavenumber SSH components from SWOT improve the gravity accuracies (SSH_model (along & cross) Vs. SSH_DTU18) by 2.4% to 20.2% with a mean of 3.4%. However, there are several lines with negative Rate1 values (magnitudes below 10%). In these cases, the use of the SWOT SSHs may have resulted in high-frequency gravity oscillations to cause the negative Rate1 values.

Unlike conventional altimeters, which can only observe one-dimensional, along-track SSHs, SWOT can deliver two-dimensional data for obtaining along- and cross-track SSHs. The cross-track SSHs can improve the accuracy of altimeter-derived gravity anomaly. For example, Fig. 11 (b) and (c) (for L12 and L17) show that gravity anomalies derived from only the along-track SSHs (magenta lines) are smoother than those (blue dashed lines) derived from both the along- and cross-track SSHs. The smoothness or weakened gravity signal along these ship lines is due to the lack of east gradient components in the along-track only case. Table 1 shows that along L12 and L17, the accuracies of gravity anomalies in the along- and cross-track case are higher than those in the along-track only case. Table 2 shows the gravity accuracy improvement due to cross-track SSHs, represented by the value of Rate2 $= \frac{RMS_{SSH\_model(along)} - RMS_{SSH\_model(along\&cross)}}{RMS_{SSH\_model(along)}} \times 100\%$ (a positive Rate2 value suggests improvement). Table 2 shows that the use of cross-track SSHs results in positive Rate2 in most lines with a mean Rate2 value of 2.2%.

The SWOT errors can mask the GG signals. This signal masking can be seen by comparing the residual along-track GGs in Fig. 12 (a) and Fig. 12 (c), and by comparing the residual cross-track GGs in Fig. 12 (b) and (d). Furthermore, compared with the simulated SWOT errors (Fig. 8 (a)), the patterns of residual GGs in Fig. 12 (c) and (d) are different from those in Fig. 8 (a). This is because the systematic errors in Fig. 8 (a) were largely removed when calculating the residual GGs, leaving only random errors. For the two swaths of each nadir track, the random errors in Fig. 12 (c) and (d) increase with the distance from the nadir track. This is a result that is predicted by the simulations in Section 3.2. Thus, we removed the SSH observations within 4 km to the edges of the swaths. Removing such data at the 4-km edges can avoid erroneous gravity anomalies recovered from SWOT observations, but widens the SSH data gaps (Fig. 12 (c) and (d) Vs. Fig. 12 (e) and (f)). The gaps can be filled by SSHs from (1) non-repeat SWOT orbits (if available), or (2) conventional altimeters (especially GM missions), or (3) simply interpolations from SSHs neighboring to the gaps from the 21-day repeat SWOT orbits.

Using one cycle of SWOT observations, we have shown that the high-wavenumber SSH components (from the residual depths) and the cross-track GGs can improve the accuracy of gravity anomalies derived from SWOT. Next, we experimented with 19 cycles of SWOT data to examine noise suppression by stacking SSH observations. First, we used one-dimensional filtering to filter the along-track data. Note that the cross-track errors vary across the swath and are difficult to be reduced. Our

Table 2
RMS differences between the IVM-derived gravity anomalies and the shipborne gravity anomalies (unit: mgal, except for Rate1 and Rate2).

Line	SSH_DTU18 (one cycle)	SSH_model (one cycle)				19-cycle SSH_obs	
		Along	Along & cross	Rate1(%)	Rate2(%)	Mean[a] SSH	Mean[b] gradient
L1	2.08	2.17	1.95	5.92	9.83	1.87	1.86
L2	2.03	1.94	2.17	−6.89	−11.84	2.12	2.14
L3	2.16	1.76	1.91	11.68	−8.60	1.77	1.75
L4	1.98	1.81	2.15	−8.48	−18.47	2.04	2.06
L5	3.19	3.06	3.11	2.42	−1.57	3.02	3.07
L6	2.91	2.85	2.81	3.27	1.12	2.77	2.77
L7	1.82	1.88	1.95	−7.10	−3.51	1.97	1.96
L8	1.85	2.11	2.00	−7.89	5.13	1.93	1.92
L9	2.97	3.02	2.77	7.00	8.47	2.70	2.68
L10	2.84	3.22	2.71	4.89	15.86	2.70	2.68
L11	2.31	2.52	2.25	2.56	10.68	2.08	2.14
L12	2.72	2.49	2.30	15.64	7.71	2.38	2.39
L13	2.44	2.39	2.01	17.43	15.80	1.94	1.91
L14	3.29	3.01	3.34	−1.67	−10.99	2.63	2.64
L15	3.89	3.97	4.00	−2.82	−0.93	3.87	3.89
L16	2.66	2.96	2.56	3.65	13.49	2.40	2.37
L17	3.49	3.50	2.78	20.21	20.50	2.96	2.79
L18	3.28	3.17	3.10	5.46	2.24	3.29	3.26
L19	2.61	2.33	2.62	−0.54	−12.43	2.47	2.49
Mean	2.66	2.64	2.55	3.41	2.24	2.47	2.46

[a] The gradients are derived from the averaged SSHs over the 19 cycles.
[b] The gradients are the averaged gradients over the gradients from the 19 cycles.

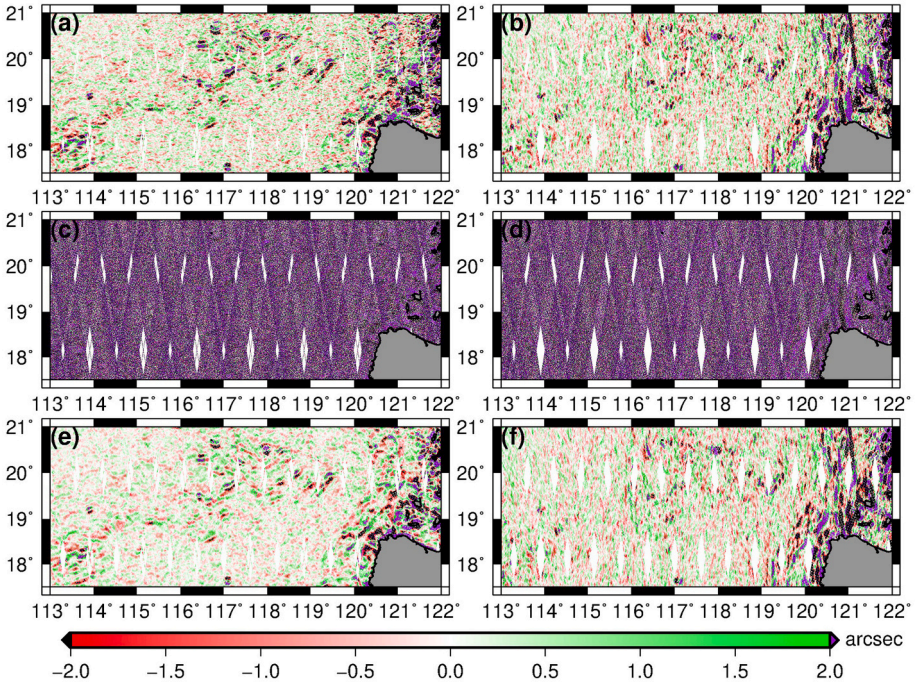

Fig. 12. (a) Residual along-track GGs, (b) residual cross-track GGs from one cycle of SSHs (SSH_model, error free), (c) residual along-track GGs, (d) residual cross-track GGs from one cycle of SSHs (SSH_obs, error contaminated), (e) residual along-track GGs, and (f) residual cross-track GGs from edge-removed, 19 cycles of SSHs.

filtering employed the function "smooth" available in MATLAB and we chose the method "lowess" that filters input data by locally weighted linear regression. Second, we used two methods to average the 19 cycles of SWOT SSH observations. In the first method (mean SSH, Table 2), we averaged the filtered SSH observations over the 19 cycles. The resulting residual (mean) along- and cross-track GGs are shown in Fig. 12 (e) and (f), respectively. In the second method (mean gradient, Table 2), we computed along- and cross-track gradients, and then averaged the gradients over the 19 cycles. The resulting residual along- and cross-track GGs (not shown in this paper) are similar to those shown in Fig. 12 (e) and (f). The GGs from the two methods were then separately used to compute gravity anomalies by IVM. Table 2 compares the accuracies of the recovered gravity anomalies by the two methods (based on mean SSH and mean gradient) and shows that the mean accuracy difference is 0.01 mgal. This suggests that errors in SWOT SSHs can be reduced by averaging (stacking) multiple cycles of SWOT data. However, we recommend using the second method for obtaining optimal GGs from multiple SWOT cycles because numerical differentiations of SSHs for GGs can reduce long-wavelength (systematic) errors in SSHs for an individual cycle before averaging over multiple cycles.

Fig. 13 (a) and (b) show the effectiveness of suppressing errors in SWOT SSH observations along L12 and L17 by the error suppression described above. The differences between the gravity anomalies from the error-suppressed SSH_obs and the original observations (green

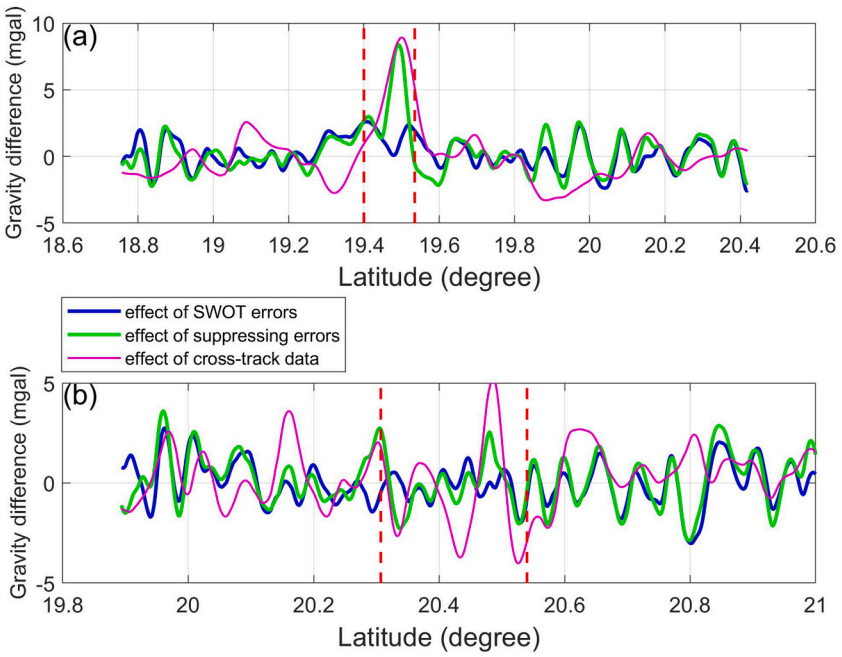

Fig. 13. The effect of SWOT errors on IVM-derived gravity anomalies, the effect of suppressing errors, and the effect of cross-track data along (a) L12 and (b) L17. The blue lines represent the differences between gravity from one-cycle SSH_obs and SSH_model and can be regarded as the effect of SWOT errors. The green lines represent the differences between gravity from one-cycle SSH_obs and from 19-cycle, error-suppressed SSH_obs and can be regarded as the effect of suppressing errors. The magenta lines represent the differences between gravity from only along-track SSH_model and along- and cross-track SSH_model and can be regarded as the effect of cross-track data. (For interpretation of the references to colour in this figure legend, the reader is referred to the web version of this article.)

lines), which can be regarded as the effect of suppressing errors, are similar to the differences between the gravity anomalies from SSH_obs and SSH_model (blue lines), which can be regarded as the effect of SWOT errors, except over a region over seamounts along L12 and L17. Over such seamount-dominated regions, the short-wavelength SSHs originating from the seamounts can also be reduced by filtering. In summary, suppressing noises can reduce the damaging effect of SWOT SSH errors on gravity accuracy. In addition, the cross-track data can

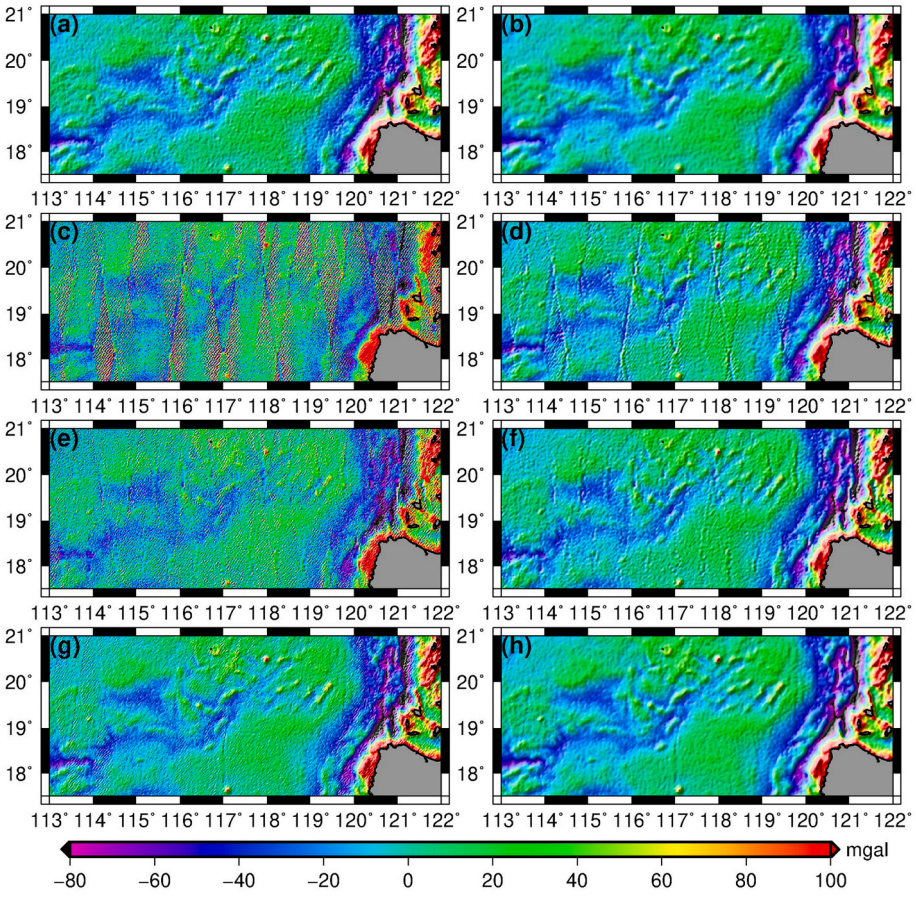

Fig. 14. ISM-derived gravity anomalies from one cycle (a to f) and 19 cycles (g and h) of SWOT SSHs. The left column shows the original gravity anomalies and the right column shows the filtered ones. (a) and (b) SSH_DTU18, (c) and (d) SSH_obs, (e) and (f) edge-removed SSH_obs, (g) and (h) 19 cycles, tilt-corrected SSH_obs.

strengthen the gravity signals (magenta lines in Fig. 13) over seamounts (signal strengthening is supported by the comparisons of blue dashed lines and magenta lines in Fig. 11 (b) and (c)).

5.2. Gravity recovery by ISM

This section shows gravity anomalies derived by ISM (Section 4.2) using simulated SWOT SSHs. We experimented with one cycle and 19 cycles of SWOT observations to investigate how the SWOT errors affect the recovered gravity and propose methods to suppress these errors. First, the effectiveness of our computer program for ISM is demonstrated using the result in Fig. 14 (a), which shows the gravity anomalies from one-cycle SSH_DTU18 by ISM. Because converting SSHs to gravity anomalies can amplify high-frequency noises in SSHs (Andersen and Knudsen, 1996), we filtered the initial gravity anomalies by the Gauss filter, as shown in Fig. 14 (b). Table 3 shows the RMS differences between the shipborne gravity anomalies and those from SSHs (by ISM) in various cases. In particular, the RMS differences in the case of filtered gravity from SSH_DTU18 are close to or even smaller than those of the DTU17 gravity. These results suggest that our computer program for the inverse Stokes' integral and the innermost-zone effect work properly.

Fig. 14 (c) shows the gravity anomalies from one cycle SSH_obs by ISM. Evident stripe and zigzag structures are present in Fig. 14 (c) and are the result of the SWOT SSH errors. The RMS differences between the ISM-derived gravity anomalies from SSH_obs and the shipborne measurements are larger than 10 mgal along all lines (Table 3), implying that the use of error-contaminated SWOT SSHs in ISM will result in marine gravity anomalies with unacceptably large errors (>10 mgal). We then filtered such gravity anomalies by the Gauss filter, and the result (Fig. 14 (d)) is free from the zigzag structures but still contains the gravity stripes.

Here, we propose a method to mitigate the effect of SWOT SSH errors on ISM-derived gravity by correcting the tilt in SSHs over a swath with respect to a reference surface as follows. A reference surface should be smooth and close to the original SWOT observations, or it can lead to new systematic errors in the corrected SSHs that will propagate into erroneous gravity signals. In this paper, we used the simulated SWOT observations in the study area to generate a mean sea surface on a grid, which is then smoothed to form the needed reference surface. Second, the two-dimensional SSH observations over a swath are split into one-dimensional cross-track observations, as shown in Fig. B1 Third, for each across track, the differences between the original SSH observations and the SSHs from the reference surface are fitted by

$$\Delta l_i + v_i = a \bullet d_i + b \tag{19}$$

where Δl_i is the difference between the original SWOT SSH and the reference SSH, d_i is the distance from the nadir track, v_i is the residual, and a and b are the coefficients correcting the bias and tilt in SSHs along the cross-track direction. The coefficients a and b were estimated by the least-squares method. The corrected SWOT observations are called tilt-corrected SSH_obs.

Fig. 14 (e) shows the ISM-derived gravity from one-cycle tilt-corrected SSH_obs without using SSHs at the swath edges. By correcting the tilted SSHs over swaths, the zigzag structures are weakened. After Gauss filtering the gravity in Fig. 14 (e), the zigzag structures almost disappear in the result, as shown in Fig. 14 (f), but the gravity stripes are still present and are the result of using only one cycle of SWOT data. These experiments highlight the importance of correcting the tilted SSHs over swaths and post-filtering when recovering gravity anomalies using GHs and by ISM.

It turns out filtering is a critical procedure for deriving high-quality gravity anomalies by ISM. As shown in Fig. 15 (a) and (b) along L12 and L17, the filtered gravity anomalies from SSH_model (black lines) are much smoother and more consistent with the shipborne gravity values than the un-smoothed ones (green lines). In the comparisons in Fig. 15 (a) and (b), it is remarkable that the black lines (filtered gravity from SSH_model) conform to the cyan line (shipborne gravity) very well over the seamount, proving the effectiveness of filtering. Furthermore, the yellow lines in Fig. 15 (a) and (b), which represent the gravity anomalies derived from SSH_obs, oscillate rapidly due to the SSH noise amplification effect when converting GHs to gravity anomalies by ISM. The amplification is due to the fact that the spectral content gravity anomaly is one order higher than GH (Rummel, 1997).

Our experiments indicate that gravity anomalies by ISM from one cycle of SWOT observations contain gravity artifacts. To reduce such gravity artifacts when using ISM, one should use multiple cycles of SWOT observations. To this end, we averaged the SSHs from 19 cycles of SWOT data and created an improved reference surface, which was then used for correcting the tilts of swaths. The recovered gravity field from 19-cycle, tilt-corrected SWOT SSHs (without filtering) is shown in Fig. 14 (g), which contains less gravity zigzag and stripe structures than those present in Fig. 14 (e). The filtered gravity field from the multiple-cycle SWOT data (Fig. 14 (h)) is similar to that in Fig. 14 (b). Table 3 shows that the accuracy of the filtered gravity from the 19-cycle data is close to the accuracy of the DTU17 gravity. The accuracy improvement by using multiple cycles of SWOT SSHs is also confirmed by the comparisons of gravity anomaly profiles from 19 cycle (magenta dashed lines) and shipborne gravity anomalies along L12 and L17 in Fig. 15 (a) and (b).

Table 3
RMS differences between the ISM-derived gravity anomalies and the shipborne gravity anomalies (unit: mgal).

Line	DTU17 gravity	SSH_DTU18 (one cycle)		SSH_obs (one cycle, before filter)	19-cycle SSH_obs	
		Before filter	After filter		Before filter	After filter
L1	1.89	2.93	2.17	17.00	7.62	2.82
L2	1.82	2.36	1.82	43.80	5.52	2.23
L3	1.78	2.51	1.92	36.16	4.90	1.68
L4	1.65	2.45	1.73	38.00	5.97	2.14
L5	3.09	3.81	3.22	22.20	5.37	3.25
L6	2.63	3.61	2.79	41.76	7.39	3.12
L7	1.53	2.12	1.72	27.59	4.94	2.54
L8	2.12	2.17	1.57	44.88	5.37	1.98
L9	3.04	3.46	2.78	40.12	5.68	2.49
L10	3.25	3.11	2.73	26.12	4.97	2.79
L11	2.36	3.08	2.23	28.71	5.93	2.29
L12	2.51	3.35	2.88	39.19	6.67	2.49
L13	2.48	3.45	2.72	34.14	5.56	2.41
L14	3.58	3.71	3.10	20.53	6.58	3.07
L15	3.84	4.05	3.67	32.44	6.90	3.77
L16	2.73	3.27	2.64	29.74	5.84	2.34
L17	3.38	3.73	2.91	36.84	5.50	2.59
L18	2.84	4.11	3.24	38.78	4.87	3.38
L19	2.41	4.26	3.01	36.98	5.22	2.86

6. Discussion and method summary

6.1. Sensitivities of IVM and ISM to SWOT errors

This paper investigates the potential of SWOT SSH observations in recovering marine gravity anomalies. The results given in Section 5 (Table 1, Table 2, Fig. 10 and Fig. 11) show that SWOT SSH observations can contribute to the detection of seamounts and other high-frequency seafloor features not present (at least with lesser magnitudes) in the latest gravity fields from conventional altimeters such as DTU18 and Version 30.1 of Sandwell and Smith (1997).

For cross-validation, two independent methods (IVM and ISM) and data types (GG and GH) are used to recover marine gravity anomalies. The results from one cycle of SWOT observations in Table 2 and Table 3 show that the gravity accuracies from these two methods are similar when the SWOT SSH errors were not present. However, when the SSH

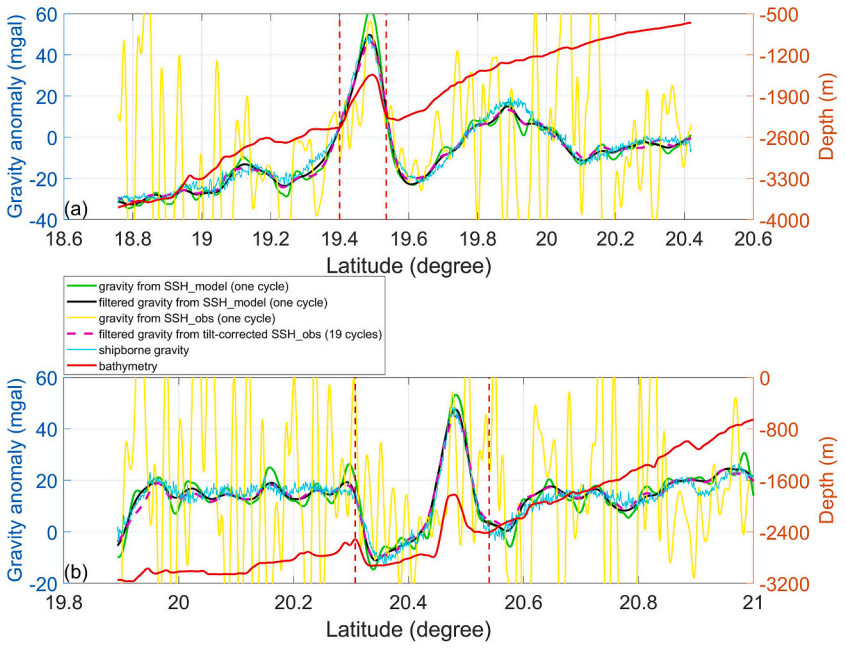

Fig. 15. (a) Depths and ISM-derived gravity anomalies along L12, and (b) L17 from one cycle and 19 cycles of SWOT SSHs.

errors were introduced, they did have impacts on the recovered gravity anomalies. The IVM-derived gravity anomalies are smooth and close to the shipborne gravity anomalies (yellow lines in Fig. 11 (b) and (c)). In contrast, the ISM-derived gravity anomalies undergo large variations (yellow lines in Fig. 15) and show the gravity accuracies can be larger than tens of mgal (Table 3). It is clear the two methods are affected by SWOT SSH errors in different ways.

IVM can eliminate systematic errors, especially those due to the SSH

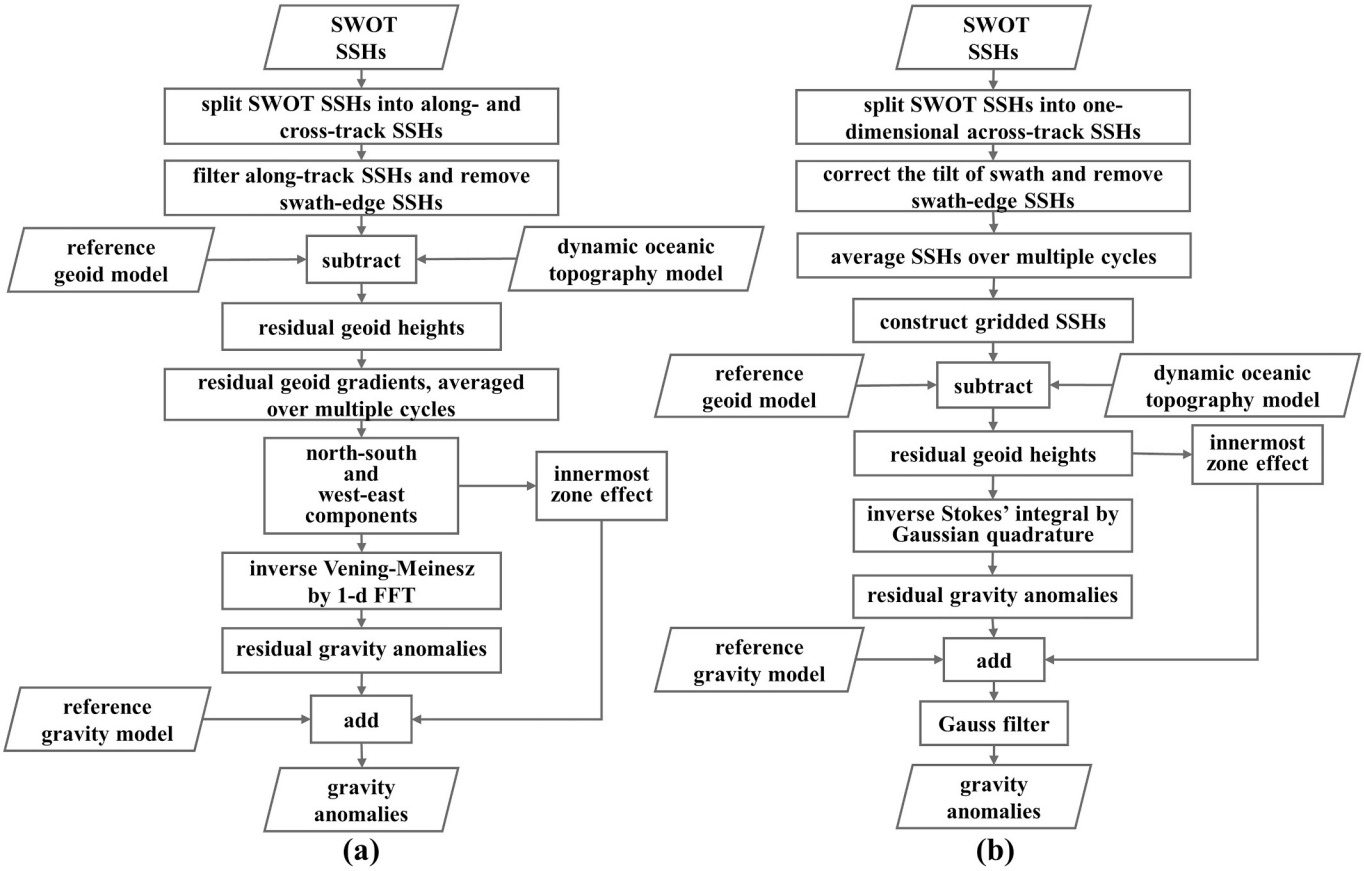

Fig. 16. Summaries of gravity recovery procedures by (a) IVM, and (b) ISM. Note that averaging over multiple cycles is carried out in different ways for IVM and ISM.

tilts over swaths because a GG is formed by differencing two successive GHs affected by nearly the same systematic errors. Although the SWOT observation errors obscure residual along-track GGs (Fig. 12 (c) and (d)), most of the original gravity signals can be recovered by IVM (yellow lines in Fig. 11 (b) and (c)). In contrast, ISM cannot remove the tilt effects and reduce the noise amplifications without pre-processing (tilt removal) and filtering (post-processing). Without a careful data processing, ISM can result in a gravity field not reflecting seafloor features. In summary, IVM is a more robust method than ISM when SWOT observation errors are present.

6.2. Summary of gravity recovery procedures

From the results in Section 5, for IVM and ISM we propose an optimal data processing procedure for gravity recovery using SWOT SSHs as follows. When using GGs from SWOT SSHs to derive gravity anomalies by IVM, the suggested processing strategy is shown in Fig. 16 (a). The pre-processing of SWOT observations consists of three steps. First, the wide-swath observations are split into along- and cross-track observations to prepare for generating GGs. Second, a smoothing function such as the one from MATLAB used in this study should be employed to filter the high-frequency noises of SWOT SSHs, because IVM can only eliminate most of the systematic errors in SWOT SSHs. Third, the SWOT observations or GGs from such observations should be averaged over multiple cycles to further mitigate the SWOT errors.

To recover useful gravity anomalies from error-contaminated GHs from SWOT by ISM, the SWOT SSH errors should be eliminated as much as possible because the ISM proposed in this paper demands highly accurate gridded GHs. To remove the tilt of swath and the noise-amplification effect on gravity, the SWOT observations have to be split into cross-track observations. Note that we do not consider the location error resulting from the SWOT observation errors. This is because the largest height error in Fig. 8 (a) is about 0.2 m, which will induce a location error (lateral change) that is far smaller than the grid interval (2 km in this paper) in this extreme case. Averaging the SWOT SSHs over multiple cycles can further reduce the errors, and can also create a better smooth reference surface than that based on just a single cycle. For each cycle, the biases and slopes with respect to the reference surface over a swath should be removed by, e.g., the regression method given in Section 5.2. Note that, an alternative method for eliminating SWOT SSH errors is proposed by Gómez-Navarro et al. (2020, 2018) for non-gravity applications.

It is planned that the SWOT Level 2 ocean products will provide the SSHs on a 2-km grid and a ~ 250 m native grid (Stiles, 2020). The SSHs will be improved by corrections for instrument errors and dry and wet tropospheric delays, sea state bias, and ionospheric delay. The 250-m grid product is intended for expert users who can resample and spatially smooth the original SSHs to obtain a desired spatial resolution. However, such corrections may still lead to SSHs that are unsatisfactory for users, thus the proposed procedures in Fig. 16 may be needed to recover an optimal gravity field.

6.3. Prospect for validation in the fast-sampling phase

Our data processing procedures for gravity recovery can be employed to validate the observed SSHs in the fast-sampling phase of SWOT (Morrow et al., 2019b) in early 2022. Fig. 17 (a) shows that a ground track in this phase will pass through the western SCS, traveling from Hainan Island (southern China) to northern Borneo Island (Malaysia). The two swaths on the two sides of this pass will cover a region of rough gravity field (see the background gravity anomalies) and energetic oceanic eddies (Chu et al., 2020). Fig. 17 (b) shows the shipborne gravity anomalies from the National Centers for Environmental Information (NCEI; https://www.ngdc.noaa.gov), which can be used to validate the gravity anomalies recovered from the SWOT SSHs over the two swaths. The fast-sampling phase will provide daily SSHs for 90 days in the two swaths in Fig. 17 (a). The averaged SSHs from the 90-day data will reduce the SSH noises by $\sqrt{90} = 9.5$, and allow inspecting how the tilts of SSHs over the swaths behave from one day to another and allow developing strategies for dealing with such tilts for a best gravity

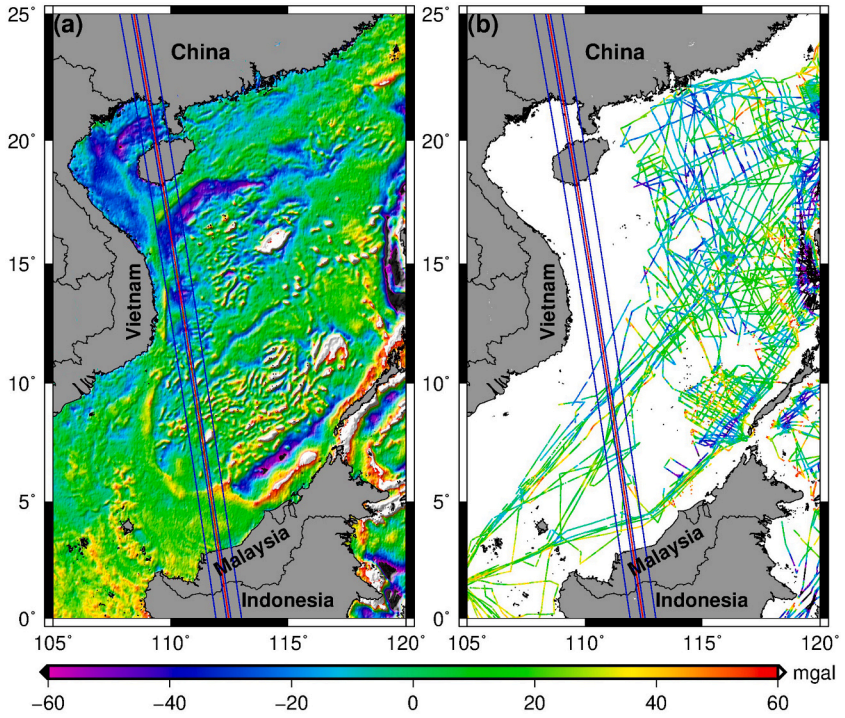

Fig. 17. (a) The ground track of pass 8 (red line) and its neighboring swaths (enclosed by two blue lines) in the SWOT fast-sampling phase in the western South China Sea. The background gravity anomalies are from the DTU17 gravity. (b) Shipborne gravity anomalies from NCEI. (For interpretation of the references to colour in this figure legend, the reader is referred to the web version of this article.)

recovery and a best oceanic eddy identification.

7. Conclusion

In this study, we realistically mimic the high-wavenumber SSH components from multi-beam depths by the concept of RDM, which are the continuous and homogeneous SSH signals. The SWOT observation errors are simulated by the SWOT simulator. We show that the SWOT wide-swath observations can indeed contribute to the recovery of marine gravity anomalies at an accuracy that cannot be achieved by conventional, nadir-looking altimeters.

The two computational methods, IVM and ISM, are rigorously implemented in this paper and consider the innermost-zone effect. Both methods can recover gravity anomalies with a similar accuracy when the SWOT errors are not present. However, the two methods have different sensitivities to SWOT errors. While IVM can easily eliminate systematic errors in SWOT SSHs, ISM demands more pre-processing and post-processing works to obtain a reliable gravity field from error-contaminated SWOT SSHs. The tilt of swath is the most damaging error for gravity derivation using ISM and GHs. Averaging multiple cycles of SWOT observations can suppress errors and improve the accuracies of gravity anomalies over the results of using just one cycle of SWOT data. Cross-validating gravity anomalies from these two independent methods can avoid artificial gravity signals that can lead to incorrect geophysical interpretations.

Using the results of the experiments conducted in this paper, we recommend the data processing strategies when using GGs and GHs to recover marine gravity anomalies. The proposed strategies can be employed to process and validate the SWOT data from the fast-sampling phase (one-day repeat period) and the nominal/science phase (21-day repeat period) to convince the scientific community that SWOT can indeed revolutionize the potency of satellite altimetry in marine gravity recovery.

Author contributions

C. Hwang and D. Yu conceptualized the initial idea and experimental design. D. Yu made all computations and wrote the first draft with C. Hwang. O. B. Andersen, E. T.Y. Chang, and L. Gaultier reviewed and edited the draft.

Declaration of Competing Interest

The authors declare that we have no conflict of interest.

Acknowledgments

This study is supported by Ministry of Science and Technology, Taiwan, under grant numbers: 109-2611-M-009-001, 109-2221-E-009-015-MY3, and 109-2611-M-002-012. Supports to O. B. Andersen and L. Gaultier under SWOT projects are acknowledged. All the computer programs developed in this paper are free for use to test observations from SWOT.

Appendix A. List of abbreviations

CNES	Centre National d'Études Spatiales
DOT	dynamic oceanic topography
DOV	deflection of the vertical
DTU18MSS	DTU18 mean sea surface
ERM	Exact Repeat Missions
FFT	fast Fourier transform
GEBCO	General Bathymetric Chart of the Oceans
GG	geoid gradient
GH	geoid height
GM	geodetic mission
ISM	method of inverse Stokes' integral
IMSL	International Mathematical and Statistical Library
IVM	method of inverse Vening-Meinesz
KaRIN	Ka-band Radar Interferometer
LSC	least-squares collocation
MOI	Ministry of the Interior
MSS	mean sea surface
NASA	National Aeronautics and Space Administration
RDM	residual depth model
RMS	root-mean-squared
RTM	residual terrain model
SAR	synthetic aperture radar
SCS	South China Sea
SSH	sea surface height
SSH_DTU18	error-free SWOT observations from DTU18MSS model
SSH_model	error-free SWOT observations from the combination of DTU18MSS model and high-wavenumber SSHs
SSH_obs	error-contaminated SWOT observations from SSH_model
SWOT	Surface Water and Ocean Topography

Appendix B. Forming north and east gradient components using least-squares collocation

Future SWOT SSHs will be given over swaths, instead of along-track points. To use IVM for gravity recovery from SWOT SSHs, first, we split the SSHs in the two swaths on the two sides of a given nadir track into along- and cross-track SSHs with a 2-km spacing. Fig. B1 shows this concept of splitting. Next, we use the LSC method to calculate the north and east gradient components from GGs using

$$\mathrm{s} = \begin{pmatrix} \xi \\ \eta \end{pmatrix} = C_{sL}(C_{LL} + D_L)^{-1} L \tag{A1}$$

where L is a vector containing residual GGs calculated by Eq. (8), s is a vector containing north (ξ) and east (η) gradient components, D_L works as a filter and is a diagonal matrix containing the noise variances of GGs, and C_{sL} and C_{LL} are covariance matrices for north (or east) gradient component-gradient and gradient-gradient. The diagonal elements of $(C_{LL} + D_L)$ contain the error variances of EGM2008 and the error variances of residual GGs (based on a 0.04-m SSH error).

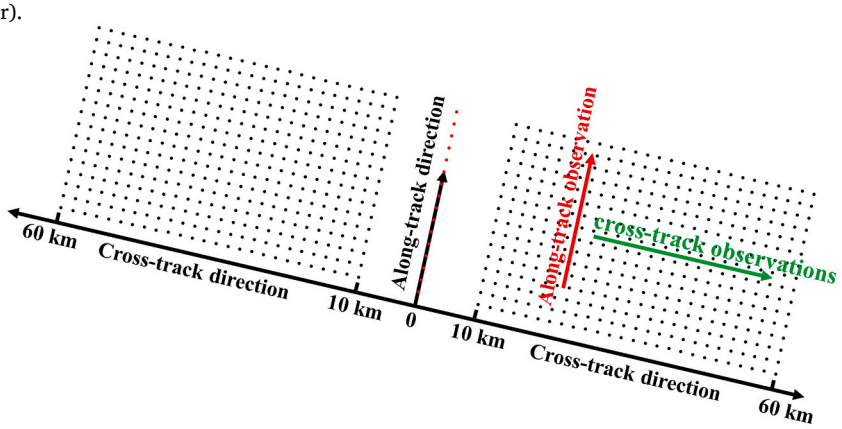

Fig. B1. Diagram of the SWOT grid points at 2-km resolution and the along- and cross-track observations split from the two-dimensional swath observations.

C_{LL} consists of the gradient covariance of any two points in vector L. For example, two points, P and Q, are shown in Fig. B2 with the geoid gradients of ε_P and ε_Q, respectively. The longitudinal and transverse components of ε_P and ε_Q are l and m. The direction of l is from P to Q, and m is perpendicular to l. The geoid gradients can be expressed in terms of (l, m) as (Hwang and Parsons, 1995)

$$\varepsilon_P = l\bullet\cos\left(\alpha_{\varepsilon_P} - \alpha_{PQ}\right) + m\bullet\sin\left(\alpha_{\varepsilon_P} - \alpha_{PQ}\right) \tag{A2}$$

$$\varepsilon_Q = l\bullet\cos\left(\alpha_{\varepsilon_Q} - \alpha_l\right) + m\bullet\sin\left(\alpha_{\varepsilon_Q} - \alpha_l\right) = -l\bullet\cos\left(\alpha_{\varepsilon_Q} - \alpha_{QP}\right) - m\bullet\sin\left(\alpha_{\varepsilon_Q} - \alpha_{QP}\right) \tag{A3}$$

Because cov(l, m) = 0, the covariance between ε_P and ε_Q is

$$C_{\varepsilon_P\varepsilon_Q} = cov(\varepsilon_P, \varepsilon_Q) = -C_{ll}cos(\alpha_{\varepsilon_P} - \alpha_{PQ})cos\left(\alpha_{\varepsilon_Q} - \alpha_{QP}\right) - C_{mm}\, sin(\alpha_{\varepsilon_P} - \alpha_{PQ})sin\left(\alpha_{\varepsilon_Q} - \alpha_{QP}\right) \tag{A4}$$

If P and Q are close, we can assume $\alpha_{QP} = \alpha_{PQ} + \pi$. This assumption leads to

$$C_{\varepsilon_P\varepsilon_Q} = C_{ll}\bullet\cos\left(\alpha_{\varepsilon_P} - \alpha_{PQ}\right)\bullet\cos\left(\alpha_{\varepsilon_Q} - \alpha_{PQ}\right) + C_{mm}\bullet\sin\left(\alpha_{\varepsilon_P} - \alpha_{PQ}\right)\bullet\sin\left(\alpha_{\varepsilon_Q} - \alpha_{PQ}\right) \tag{A5}$$

The elements of C_{LL} are the covariances computed using Eq. (A5) for all pairs of gradients from SWOT in a data window. The elements of C_{sL} are the covariances between the north (azimuth 0°) and east gradient (azimuth 90°) components and all gradients in the data window.

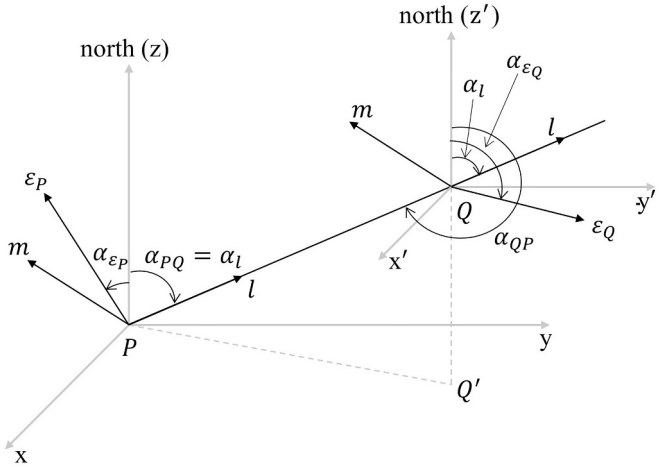

Fig. B2. Illustration of the longitudinal and traverse gradient components used in calculating gradient covariance between points P and Q (Hwang and Parsons, 1995).

Appendix C. Implementing the inverse Stokes' integral by Gaussian quadrature

The ISM method requires the inverse Stokes' integral to be numerically evaluated. This paper uses the Gaussian quadrature to evaluate this integral with the input from re-sampled, gridded SSHs from SWOT. Using $l_0 = 2Rsin(\Psi_{PQ}/2)$ in the inverse Stokes' integral (Eq. (12)), we have

$$\Delta g_P = -\frac{\gamma_P N_P}{R} - \frac{\gamma_P R^2}{2\pi}\iint_\sigma \frac{N_Q - N_P}{l_0^3}d\sigma_Q = -\frac{\gamma_P N_P}{R} - \frac{\gamma_P}{16\pi R}\iint_\sigma \frac{N_Q - N_P}{sin^3(\Psi_{PQ}/2)}d\sigma_Q \tag{A6}$$

where

$$sin\left(\frac{\Psi_{PQ}}{2}\right)=\frac{sin(\Psi_{PQ})}{2cos(\Psi_{PQ}/2)}=\frac{sin(\Psi_{PQ})}{2\sqrt{\frac{1+cos(\Psi_{PQ})}{2}}}=\frac{\sqrt{1-cos^2(\Psi_{PQ})}}{\sqrt{2(1+cos(\Psi_{PQ}))}}=\sqrt{\frac{1-cos(\Psi_{PQ})}{2}} \tag{A7}$$

Eq. (A6) can be expressed by

$$\Delta g_P=-\frac{\gamma_P N_P}{R}-\frac{\gamma_P}{4\sqrt{2}\pi R}\iint_{\sigma}(N_Q-N_P)(1-cos(\Psi_{PQ}))^{-\frac{3}{2}}d\sigma_Q \tag{A8}$$

where

$$cos(\Psi_{PQ})=sin(\varphi_P)sin(\varphi_Q)+cos(\varphi_P)cos(\varphi_Q)cos(\lambda_Q-\lambda_P) \tag{A9}$$

The areal element $d\sigma_Q$ can be expressed by

$$d\sigma_Q=cos(\varphi)d\varphi d\lambda \tag{A10}$$

Using the expressions in Eq. (A9) and Eq. (A10) for Eq. (A8), we have:

$$\Delta g_P=-\frac{\gamma_P N_P}{R}-\frac{\gamma_P}{4\sqrt{2}\pi R}\int_{\varphi}\int_{\lambda}f(\lambda,\varphi)d\lambda d\varphi \tag{A11}$$

For a given area bounded by λ_1 (west), λ_2 (east), φ_1 (south), φ_2 (north), Eq. (A11) can be evaluated numerically by

$$\Delta g_P=-\frac{\gamma_P N_P}{R}-\frac{\gamma_P}{4\sqrt{2}\pi R}\int_{\varphi_1}^{\varphi_2}\int_{\lambda_1}^{\lambda_2}f(\lambda,\varphi)d\lambda d\varphi\approx-\frac{\gamma_P N_P}{R}-\frac{\gamma_P}{4\sqrt{2}\pi R}\sum_{j=1}^{M}w_j^{\varphi}c(\varphi_j) \tag{A12}$$

where

$$c(\varphi)=\int_{\lambda_1}^{\lambda_2}f(\lambda,\varphi)d\lambda\approx\sum_{i=1}^{N}w_i^{\lambda}f(\lambda_i,\varphi) \tag{A13}$$

where w_i^{λ} and w_j^{φ} are weighting coefficients, λ_i and φ_j are nodal coordinates, M and N are the numbers of weighting coefficients and nodes along the λ and φ axes over the domains $[\lambda_1, \lambda_2]$ and $[\varphi_1, \varphi_2]$. Because the input geoid heights in this paper are given on a regular geographic grid, the function values $c(\varphi)$ and $f(\lambda,\varphi)$ at the nodes λ_i and φ_j can be interpolated using the Newton-Gregory forward polynomial (Gerald, 2004).

References

Andersen, O.B., Knudsen, P., 1996. Altimetric gravity field from the full ERS-1 geodetic mission. Phys. Chem. Earth 21, 337–341. https://doi.org/10.1016/S0079-1946(97)00058-X.

Andersen, O.B., Knudsen, P., 1998. Global marine gravity field from the ERS-1 and Geosat geodetic mission altimetry. J. Geophys. Res. 103, 8129–8137.

Andersen, O.B., Knudsen, P., 2019. The DTU17 global marine gravity field: First validation results. In: Mertikas, S.P., Pail, R. (Eds.), Fiducial Reference Measurements for Altimetry. Springer International Publishing, Cham, pp. 83–87.

Andersen, O.B., Knudsen, P., Berry, P.A.M., 2010. The DNSC08GRA global marine gravity field from double retracked satellite altimetry. J. Geod. 84, 191–199. https://doi.org/10.1007/s00190-009-0355-9.

Biancamaria, S., Mognard, N.M., Oudin, Y., Andreadis, K.M., Clark, E.A., Lettenmaier, D. P., Durand, M., Alsdorf, D.E., Rodriguez, E., Alsdorf, D.E., 2010. Preliminary characterization of SWOT hydrology error budget and global capabilities. IEEE J. Sel. Top. Appl. Earth Obs. Remote Sens. 3, 6–19. https://doi.org/10.1109/JSTARS.2009.2034614.

Chu, X., Chen, G., Qi, Y., 2020. Periodic mesoscale eddies in the South China Sea. J. Geophys. Res. Ocean. 125, 1–15. https://doi.org/10.1029/2019JC015139.

D'Addezio, J.M., Smith, S., Jacobs, G.A., Helber, R.W., Rowley, C., Souopgui, I., Carrier, M.J., 2019. Quantifying wavelengths constrained by simulated SWOT observations in a submesoscale resolving ocean analysis/forecasting system. Ocean Model 135, 40–55. https://doi.org/10.1016/j.ocemod.2019.02.001.

Durand, M., Andreadis, K.M., Alsdorf, D.E., Lettenmaier, D.P., Moller, D., Wilson, M., 2008. Estimation of bathymetric depth and slope from data assimilation of swath altimetry into a hydrodynamic model. Geophys. Res. Lett. 35, 1–5. https://doi.org/10.1029/2008GL034150.

Elmer, N.J., Hain, C., Hossain, F., Desroches, D., Pottier, C., 2020. Generating proxy SWOT water surface elevations using WRF-hydro and the CNES SWOT hydrology simulator. Water Resour. Res. 56, 1–15. https://doi.org/10.1029/2020WR027464.

Escudier, R., Bouffard, J., Pascual, A., Poulain, P.M., Pujol, M.I., 2013. Improvement of coastal and mesoscale observation from space: application to the northwestern Mediterranean Sea. Geophys. Res. Lett. 40, 2148–2153. https://doi.org/10.1002/grl.50324.

Esteban-Fernandez, D., 2017. SWOT Project Mission Performance and Error Budget. Jet Propuls. Lab. Doc. D-79084 Revis. A.

Forsberg, R., 1984. A Study of Terrain Reductions, Density Anomalies and Geophysical Inversion Methods in Gravity Field Modelling. Ohio State Univ Columbus Dept Of Geodetic Science and Surveying.

Forsberg, R., Sideris, M.G., 1993. Geoid computations by the multi-band spherical FFT approach. Manuscripta Geod. 18, 82–90.

Forsberg, R., Solheim, D., 1989. Performance of FFT Methods in Local Gravity Field Modelling. Progress in the Determination of the Earth's Gravity Field, Chapman.

Frasson, R.P. de M., Wei, R., Durand, M., Minear, J.T., Domeneghetti, A., Schumann, G., Williams, B.A., Rodriguez, E., Picamilh, C., Lion, C., Pavelsky, T., Garambois, P.-A., 2017. Automated River reach definition strategies: applications for the surface water and ocean topography Mission. Water Resour. Res. 53, 8164–8186. https://doi.org/10.1002/2017WR020887.

Fu, L.-L., Cazenave, A., 2000. Satellite Altimetry and Earth Sciences: A Handbook of Techniques and Applications. Elsevier.

Fu, L.L., Ubelmann, C., 2014. On the transition from profile altimeter to swath altimeter for observing global ocean surface topography. J. Atmos. Ocean. Technol. 31, 560–568. https://doi.org/10.1175/JTECH-D-13-00109.1.

Gaultier, L., Ubelmann, C., Fu, L.L., 2016. The challenge of using future SWOT data for oceanic field reconstruction. J. Atmos. Ocean. Technol. 33, 119–126. https://doi.org/10.1175/JTECH-D-15-0160.1.

Gaultier, L., Ubelmann, C., Fu, L.-L., 2017. SWOT Simulator Documentation. Rapp. Tech. JPL, NASA.

Gerald, C.F., 2004. Applied Numerical Analysis. Pearson Education India.

Gómez-Navarro, L., Fablet, R., Mason, E., Pascual, A., Mourre, B., Cosme, E., Sommer, J., 2018. SWOT spatial scales in the western Mediterranean Sea derived from pseudo-observations and an Ad Hoc filtering. Remote Sens. 10, 1–30. https://doi.org/10.3390/rs10040599.

Gómez-Navarro, L., Cosme, E., LeSommer, J., Papadakis, N., Pascual, A., 2020. Development of an image de-noising method in preparation for the surfacewater and ocean topography satellite mission. Remote Sens. 12, 1–24. https://doi.org/10.3390/rs12040734.

Heiskanen, W.A., Moritz, H., 1967. Physical Geodesy. Freeman WH, San Francisco.

Hsiao, Y.S., Hwang, C., Cheng, Y.S., Chen, L.C., Hsu, H.J., Tsai, J.H., Liu, C.L., Wang, C. C., Liu, Y.C., Kao, Y.C., 2016. High-resolution depth and coastline over major atolls of South China Sea from satellite altimetry and imagery. Remote Sens. Environ. 176, 69–83. https://doi.org/10.1016/j.rse.2016.01.016.

Huang, Q., Long, D., Du, M., Han, Z., Han, P., 2020. Daily Continuous River discharge estimation for Ungauged basins using a hydrologic model calibrated by satellite altimetry: implications for the SWOT Mission. Water Resour. Res. 56, 1–27. https://doi.org/10.1029/2020WR027309.

Hwang, C., 1998. Inverse Vening Meinesz formula and deflection-geoid formula: applications to the predictions of gravity and geoid over the South China Sea. J. Geod. 72, 304–312. https://doi.org/10.1007/s001900050169.

Hwang, C., Parsons, B., 1995. Gravity anomalies derived from Seasat, Geosat, ERS-1 and TOPEX/POSEIDON altimetry and ship gravity: a case study over the Reykjanes ridge. Geophys. J. Int. 122, 551–568. https://doi.org/10.1111/j.1365-246X.1995.tb07013.x.

Hwang, C., Hsu, H.Y., Jang, R.J., 2002. Global mean sea surface and marine gravity anomaly from multi-satellite altimetry: applications of deflection-geoid and inverse Vening Meinesz formulae. J. Geod. 76, 407–418. https://doi.org/10.1007/s00190-002-0265-6.

Hwang, C., Wang, C.G., Hsiao, Y.S., 2003. Terrain correction computation using Gaussian quadrature. Comput. Geosci. 29, 1259–1268. https://doi.org/10.1016/j.cageo.2003.08.003.

Knudsen, P., Andersen, O.B., Tscherning, C.C., 1992. Altimetric gravity anomalies in the Norwegian-Greenland Sea - preliminary results from the ERS-1 35 days repeat mission. Geophys. Res. Lett. 19, 1795–1798. https://doi.org/10.1029/92GL01698.

Larnier, K., Monnier, J., Garambois, P.A., Verley, J., 2020. River discharge and bathymetry estimation from SWOT altimetry measurements. Inverse Probl. Sci. Eng. 1–31. https://doi.org/10.1080/17415977.2020.1803858.

Lee, C., Kou, T.-C., Chang, E., Su, C.-C., Liu, C.-S., 2016. The updated gravity anomaly model of the south offshore Taiwan. Bull. Cent. Geol. Surv. 77-98 (in Chinese).

Lee, H., Durand, M., Jung, H.C., Alsdorf, D., Shum, C.K., Sheng, Y., 2010. Characterization of surface water storage changes in Arctic lakes using simulated SWOT measurements. Int. J. Remote Sens. 31, 3931–3953. https://doi.org/10.1080/01431161.2010.483494.

Levitus, S., Monterey, G.I., Boyer, T.P., 1997. Seasonal variability of dynamic height and its Fourier analysis. In: NOAA NESDIS Atlas 15. US Government Printing Office, Washington, DC.

Lopez-Radcenco, M., Pascual, A., Gomez-Navarro, L., Aissa-El-Bey, A., Fablet, R., 2018. Analog data assimilation for along-track nadiR and SWOT altimetry data in the western Mediterranean Sea. Int. Geosci. Remote Sens. Symp. 2018-July, 7684–7687. https://doi.org/10.1109/IGARSS.2018.8519089.

Louis, G., Lequentrec-Lalancette, M., Royer, J., Rouxel, D., Géli, L., Maïa, M., Faillot, M., 2010. Ocean gravity models from future satellite missions. EOS Trans. Am. Geophys. Union 91, 21–22.

Molodenskii, M.S., Eremeev, V.F., Yurkina, M.I., 1962. Methods for Study of the External Gravitation Field and Figure of the Earth. Transl. from Russ. (1960), Isr. Progr. Sci. Transl. Jerusalem.

Morrow, R., Fu, L.L., Ardhuin, F., Benkiran, M., Chapron, B., Cosme, E., D'Ovidio, F., Farrar, J.T., Gille, S.T., Lapeyre, G., LeTraon, P.Y., Pascual, A., Ponte, A., Qiu, B., Rascle, N., Ubelmann, C., Wang, J., Zaron, E., 2019a. Global observations of fine-scale ocean surface topography with the surface water and ocean topography (SWOT) Mission. Front. Mar. Sci. 6, 1–19. https://doi.org/10.3389/fmars.2019.00232.

Morrow, R., Fu, L.L., D'Ovidio, F., Farrar, J.T., 2019b. Scientists Invited to Collaborate in Satellite Mission's Debut. Eos, Washington. DC, p. 100. https://doi.org/10.1029/2019EO110423.

Olgiati, A., Balmino, G., Sarrailh, M., Green, C.M., 1995. Gravity anomalies from satellite altimetry: comparison between computation via geoid heights and via deflections of the vertical. Bull. Géodésique 69, 252–260. https://doi.org/10.1007/BF00806737.

Pavlis, N.K., Holmes, S.A., Kenyon, S.C., Factor, J.K., 2012. The development and evaluation of the earth gravitational model 2008 (EGM2008). J. Geophys. Res. Solid Earth 117. https://doi.org/10.1029/2011JB008916.

Rodriguez, E., Esteban Fernandez, D., Peral, E., Chen, C.W., De Bleser, J., Williams, B., 2018. Wide-Swath Altimetry: A Review.

Rummel, R., 1997. Spherical spectral properties of the Earth's gravitational potential and its first and second derivatives. Geod. Bound. Value Probl. View One Centim. Geoid 359–404. https://doi.org/10.1007/bfb0011710.

Sandwell, D.T., 1992. Antarctic marine gravity field from high-density satellite altimetry. Geophys. J. Int. 109, 437–448. https://doi.org/10.1111/j.1365-246X.1992.tb00106.x.

Sandwell, D.T., Smith, W.H.F., 1997. Marine gravity anomaly from Geosat and ERS 1 satellite altimetry. J. Geophys. Res. B Solid Earth 102, 10039–10054. https://doi.org/10.1029/96JB03223.

Sandwell, D.T., Smith, W.H.F., 2001. Bathymetric estimation. In: Fu, L.L., Cazenave, A. (Eds.), Satellite Altimetry and Earth Sciences: A Handbook of Techniques and Applications. Academic San Diego, pp. 441–457.

Sandwell, D.T., Harper, H., Tozer, B., Smith, W.H.F., 2019. Gravity field recovery from geodetic altimeter missions. Adv. Sp. Res. https://doi.org/10.1016/j.asr.2019.09.011.

Schwarz, K.P., Sideris, M.G., Forsberg, R., 1990. The use of FFT techniques in physical geodesy. Geophys. J. Int. 100, 485–514.

Solander, K.C., Reager, J.T., Famiglietti, J.S., 2016. How well will the surface water and ocean topography (SWOT) mission observe global reservoirs? Water Resour. Res. 52, 2123–2140. https://doi.org/10.1002/2015WR017952.

Stiles, B., 2020. Surface Water and Ocean Topography (SWOT) project SWOT Product Description. Jet Propuls. Lab. Doc. D-56407 Revis. A.

Tuozzolo, S., Lind, G., Overstreet, B., Mangano, J., Fonstad, M., Hagemann, M., Frasson, R.P.M., Larnier, K., Garambois, P.A., Monnier, J., Durand, M., 2019. Estimating river discharge with swath altimetry: a proof of concept using AirSWOT observations. Geophys. Res. Lett. 46, 1459–1466. https://doi.org/10.1029/2018GL080771.

Ubelmann, C., Fu, L.L., Brown, S., Peral, E., Esteban-Fernandez, D., 2014. The effect of atmospheric water vapor content on the performance of future wide-swath ocean altimetry measurement. J. Atmos. Ocean. Technol. 31, 1446–1454. https://doi.org/10.1175/JTECH-D-13-00179.1.

Wang, J., Fu, L.L., 2019. On the long-wavelength validation of the SWOT KaRIn measurement. J. Atmos. Ocean. Technol. 36, 843–848. https://doi.org/10.1175/JTECH-D-18-0148.1.

Wang, J., Fu, L.L., Qiu, B., Menemenlis, D., Thomas Farrar, J., Chao, Y., Thompson, A.F., Flexas, M.M., 2018. An observing system simulation experiment for the calibration and validation of the surface Water Ocean Topography Sea surface height measurement using in situ platforms. J. Atmos. Ocean. Technol. 35, 281–297. https://doi.org/10.1175/JTECH-D-17-0076.1.

Wang, Y.M., 1999. On the ellipsoidal corrections to gravity anomalies computed using the inverse stokes integral. J. Geod. 73, 29–34. https://doi.org/10.1007/s001900050215.

Wang, Y.M., 2001. GSFC00 mean sea surface, gravity anomaly, and vertical gravity gradient from satellite altimeter data. J. Geophys. Res. 106, 31167–31174.

Watts, A.B., 2001. Isostasy and Flexure of the Lithosphere. Cambridge University Press.

Watts, A.B., Tozer, B., Harper, H., Boston, B., Shillington, D.J., Dunn, R., 2020. Evaluation of shipboard and satellite-derived bathymetry and gravity data over seamounts in the Northwest Pacific Ocean. J. Geophys. Res. Solid Earth 125, 1–18. https://doi.org/10.1029/2020JB020396.

Weatherall, P., Jakobsson, M., Marks, K.M., 2014. General Bathymetric Chart of the Oceans (GEBCO)-Mapping the Global Seafloor. AGU Fall Meeting Abstracts.

Zhang, S., Sandwell, D.T., Jin, T., Li, D., 2017. Inversion of marine gravity anomalies over southeastern China seas from multi-satellite altimeter vertical deflections. J. Appl. Geophys. 137, 128–137. https://doi.org/10.1016/j.jappgeo.2016.12.014.

Zhu, C., Guo, J., Gao, J., Liu, X., Hwang, C., Yu, S., Yuan, J., Ji, B., Guan, B., 2020. Marine gravity determined from multi-satellite GM/ERM altimeter data over the South China Sea: SCSGA V1.0. J. Geod. 94 https://doi.org/10.1007/s00190-020-01378-4.